Precision Spectroscopy in 1D Optical Lattices

Diplomarbeit

zur Erlangung des Magistergrades an der
naturwissenschaftlichen Fakultät
der Leopold-Franzens-Universität Innsbruck

vorgelegt von

Sebastian Blatt

durchgeführt am JILA, Boulder
unter der Leitung von Rudolf Grimm und Jun Ye

Boulder, Juli 2005

Contents

List of Figures v

Introduction vii

Introduction vii

1 Oscillators and Feedback 1
1.1 Characterizing an oscillator . . . 1
1.2 Feedback theory and phase-locked loops . . . 4
1.2.1 Feedback theory . . . 5
1.2.2 Application to phase-locked loops . . . 7
1.2.3 Phase detector . . . 9
1.2.4 Loop filter . . . 10

2 Atomic Clocks and Precision Spectroscopy 13

3 Doppler Cooling and Magneto-Optical Traps 15
3.1 Doppler cooling . . . 15
3.1.1 Dissipative force . . . 16
3.1.2 Diffusion rate . . . 16
3.1.3 Cooling limits . . . 17
3.2 Magneto-optical traps . . . 17

4 1D Optical Lattices 21
4.1 AC Stark effect . . . 21
4.1.1 Branching ratios . . . 22
4.1.2 Introducing experimental parameters . . . 23
4.2 Separating the motion . . . 24
4.3 Longitudinal problem . . . 24
4.4 Vibrational spectroscopy . . . 28
4.5 Parametric heating . . . 29

4.5.1 Intensity Noise . . . 29
4.5.2 Phase Noise . . . 31
4.5.3 Heating Rates . . . 32
4.6 Environmental effects . . . 33
4.6.1 Doppler effect . . . 33
4.6.2 AC Stark shift (probe) . . . 34
4.6.3 AC Stark shift (blackbody) . . . 36
4.6.4 Second order Zeeman effect . . . 37
4.6.5 Gravitational shift . . . 39

5 Precision Spectroscopy in a 1D Optical Lattice 41
5.1 Atom preparation and MOT cooling . . . 41
5.2 1D optical lattice . . . 43
5.3 Spectroscopy . . . 45

6 Determining Absolute Frequency 53
6.1 Schematic . . . 54
6.2 Features and Remarks . . . 56
6.3 Frequency Multiplier . . . 57
6.3.1 Circuit . . . 57
6.3.2 Output . . . 60
6.3.3 Software . . . 61
6.4 Direct Digital Synthesis . . . 63
6.4.1 AD9854 . . . 64
6.4.2 Caveats . . . 65
6.4.3 Software: Drift Compensation . . . 67

7 Results and Outlook 71

Bibliography 75

Index 80

Acknowledgements 83

List of Figures

1.1 Oscillating voltage with varying momentaneous frequency 2
1.2 Noise power spectrum and Allan deviation 4
1.3 Negative feedback loop 5
1.4 Schematic of a Phase-Locked Loop (PLL) 7
1.5 Analog and digital phase detector output signals and capture range 9
1.6 Bode representation for loop filter transfer functions 11

2.1 Lowest singlet and triplet states of neutral strontium 14

3.1 MOT detunings 18

4.1 Motional sidebands in harmonic and anharmonic potentials 28

5.1 Sample preparation and pre-cooling, figure from Loftus *et al.* (2004a) . . . 42
5.2 Lowest singlet and triplet states of ^{87}Sr 42
5.3 AC Stark shifts for ^{87}Sr 44
5.4 Lattice and spectroscopy laser mount 45
5.5 Sideband spectrum 46
5.6 Multiple-Lorentzian sideband fit 47
5.7 Typical spectrum of $^1S_0 - {}^3P_0$ 48
5.8 Density shift 48
5.9 Magnetic shift 49
5.10 Lattice AC Stark shift 49
5.11 Lattice curvature for different ratios w_0/λ 50

6.1 Frequency counting setup 54
6.2 Frequency multiplier schematic 58
6.3 ADF4111 circuit 58
6.4 Loop filter circuit 59
6.5 Final Loop filter and VCO driver circuit 60
6.6 Frequency multiplier: spectral traces 62

6.7 SPI data transfer protocol 63
6.8 Piecewise linear frequency ramp 64
6.9 AD9854 DDS spectral traces 66
6.10 Drift compensation screenshots 68
6.11 Drift compensation data and Allan deviation 69

7.1 Comparison of results from Takamoto *et al.* (2005) and Ludlow *et al.* (2005) 72

Introduction

Measuring time has always been important to human society, but whereas it used to be good enough to know the current date or hour, today's increasingly technical societies need better standards. This is not only true for the second, but also for all other units of measurement, represented by the *système international* (SI). For example, layered semiconductors must be fabricated to specifications on the nm scale and ships would like to know their position on the earth's surface as accurately as possible to avoid nautical dangers. The length scales involved in both of these applications seem very different at first, but since the *global positioning system* (GPS) works by triangulating the ship's position from orbit, the necessary accuracy is comparable.

With the invention of clocks based on atomic phenomena in the middle of the last century, time could be measured so accurately that other units of measurement were *defined* with respect to the second. To state it bluntly, the atomic clock is the world's best caliper... and more. The combination of the leap in clock quality with cheap optical oscillators (lasers) created whole branches of technology and changed the standard of metrology to what it is today.

The question remains: Can we make it better? And if yes, should we? To answer these questions (with "Yes" and "Of course!"), we have to quantify what makes a good clock. A good clock must possess three attributes:

Accuracy It must be able to split time into pieces that match the definition of the second as well as possible.

Stability The clock must produce ticks at constant intervals. This is often confused with the first point, as an accurate clock must be stable, but a stable one need not be accurate.

Reproducibility One clock in the whole world is not enough. We need at least two to be able to measure their first two attributes, as will be explained later.

We characterize a clock by its frequency and a clock's instability is quantified by the deviation from its desired frequency over time. This quantity can be obtained by summing the squared deviations between two adjacent frequency measurements and has been accepted as the international standard to compare clocks. In the case of a clock

based on an atomic transition, this so-called *Allan deviation*[1] can be expressed as

$$\sigma_y(\tau) \approx \frac{\Delta\omega}{\pi\omega}\sqrt{\frac{T}{\tau N}}, \tag{0.1}$$

in the limit that the dominant noise source is quantum mechanical fluctuations (Itano *et al.*, 1993, Santarelli *et al.*, 1999).

This expression tells us the basic recipe for making a good atomic clock: $\Delta\omega$ is the width of the atomic resonance at frequency ω, so choosing a narrow atomic feature at a large frequency is desirable to minimize instability. Since we are probing a quantum mechanical system, just taking one measurement of duration T is not enough, we must average over many repetitions to obtain an accurate number. Correspondingly, τ is the averaging time. The occurrence of τ also tells us that we can make any accurate clock stable just by measuring long enough. Of course, this is where we gain a lot by choosing an atomic feature with large quality factor $Q := \omega/\Delta\omega$, as we can trade stability for shorter averaging times. Finally, N is the number of atoms involved in producing the clock's signal. Using more atoms is equivalent to measuring the atomic feature many times. This is again a trade-off we can make: more atoms means better stability, but controlling the experimental noise involved in measuring them gets increasingly difficult.

How do the current atomic clocks work? Let us take a look at the best atomic clock to date in the light of Eq. 0.1. The SI second is defined as an integer multiple of the oscillation period of a Cs transition. More specifically: the ground state hyperfine transition $|^2S_{1/2}F = 3\rangle \rightarrow |^2S_{1/2}F = 4\rangle$ in $^{133}_{55}$Cs ($I = \frac{7}{2}$) is probed with microwave radiation at 9 192 631 770 Hz. The exciting microwave frequency is locked to the atomic transition by measuring the transition probability and ensuring that it stays at its maximum. The oscillations of the microwave oscillator (maser) can then be counted electronically and a clock signal is produced.

However, we want to know if we can improve on the Cs standard. As mentioned before: in theory, we could always make a much better clock by choosing a narrower transition at higher frequency, e.g. a narrow optical transition like an intercombination line. The idea is not new, but what prevented the implementation of an *optical atomic clock* for many years is that counting the 10^5 times faster optical oscillations is impossible even with the best electronic device.

Technology caught up with the invention of the femtosecond-comb[2], a pulsed laser system with an interesting frequency spectrum: Looking like the teeth of a comb it has a component every few hundred MHz over a very wide range. The n-th tooth with frequency ω_n can be described in terms of two frequency parameters, the pulse repetition rate ν_r and the offset frequency ν_0, both of which are in the microwave domain

$$\omega_n = n\nu_r + \nu_0.$$

By producing a comb spectrum that spans whole octave, it is possible to beat a high-lying comb line against a frequency-doubled comb line and obtain a microwave beat note

[1] The Allan deviation will be introduced more formally and in much more detail in Section 1.1.

[2] A good summary and general reference is Ye and Cundiff (2004)

at ν_0 that can be counted electronically.

$$\omega_{2n} - \omega_m = \nu_0 \text{ for } 2n = m$$

Using a phase-locking technique (as described in Chapter 1.2) to lock the comb spectrum to the optical frequency standard ensures that the optical frequency is an exact integer multiple of the repetition rate ν_r. By counting ν_r and determining the integer multiplication factor, the fs-comb becomes the optical equivalent of a mechanical gear... with a translation ratio of 1 : 100 000. In the last five years, fs-combs have become the standard tool to directly count optical frequencies and many groups in the world have started projects towards an optical frequency standard. An atomic clock based on an optical transition with its large Q places stringent requirements on the experimental setup. Let us qualify these requirements and take a look at the difficulties involved in the making of an all optical atomic clock:

First: one needs to find an appropriate optical transition. It should be as narrow as possible and should be accessible with a commonly available laser source, e.g. a diode laser system.

Second: the particles must be prepared in an environment that is as immune as possible to external perturbations. I.e. the particles must be trapped inside a controllable potential that can be designed to the element's specific requirements. We shall develop a thorough understanding of this confinement in chapter 4. First, though, we will talk about choosing (chapter 2) and preparing an apropriate sample (chapter 3).

Third: resolving a narrow spectroscopic line requires a frequency source with an even narrower spectrum, i.e. a highly stabilized laser source.

Fourth: the optical frequency must be reduced to a microwave frequency to make electronic counting possible. As mentioned in the last Section, the tool to use is a femtosecond-comb.

The spectroscopy laser will be discussed throughout chapters 5, 6 and references therein. The absolute frequency measurement by comparing against a Cs standard via a femtosecond comb will be presented in chapter 6.

Finally, we will talk about future improvements on the measurements and new experiments in chapter 7.

Chapter 1

Oscillators and Feedback

This chapter introduces the basic vocabulary we will need when talking about oscillators and related techniques. The same principles hold true, regardless whether the oscillator is an electrical synthesizer, a pendulum clock or a laser.

1.1 Characterizing an oscillator

How good is an oscillator? This Section introduces a measure on the goodness of clocks, the *Allan variance*. The treatment in this Section follows the NIST tutorial on oscillators in Sullivan *et al.* (1990).

We are interested in oscillators producing sinusoidal output voltage with a well-defined and relatively stable frequency. We want to allow amplitude as well as phase noise, so it is reasonable to write down the oscillator's output as:

$$V(t) := V_0(1 + a(t)) \sin(\omega_0 t + \phi(t)) \tag{1.1}$$

with a *nominal frequency* ω_0, a small amplitude variation $a(t)$ and some phase fluctuation $\phi(t)$. The total accumulated phase at time t is $\Phi(t) := \omega_0 t + \phi(t)$. Without loss of generality, we will only consider amplitude normalized signals, i.e. $V_0 \equiv 1$.

For non-zero phase noise ϕ the signal's frequency is changing in time; can we define an instantaneous frequency? Consider the oscillating signal in Fig. 1.1 and assume that we measured its amplitude V_i at times t_i for $i = 1, 2$. The instantaneous frequency is defined as the sine wave of minimal frequency that we can fit through both of these data points.

The phase and amplitude noise is characterized by measuring this instantaneous frequency and looking at its changes in time. When we are talking about a clock's stability, we are actually talking about its instability, viz. its deviation from its nominal frequency. Actually, most measurement devices do not measure the instantaneous frequency directly in the above sense, but are measuring phase or counting oscillations. This fact already hints at an important fundamental "flaw": to determine the frequency of an oscillator

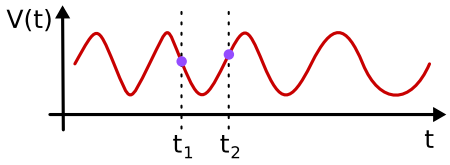

Figure 1.1: Oscillating voltage with varying momentaneous frequency

one always needs another oscillator. So all frequency (and time) measurements are relative to a reference which should ideally be much less noisy than the observed oscillator. The measurement device should also introduce less noise than the sum of both these oscillators.

It is convenient to define a fractional frequency deviation relative to the nominal frequency

$$y(t) := \frac{\omega_t - \omega_0}{\omega_0}$$

because the oscillator's *time deviation* can be expressed as its integral

$$x(t) := \int_0^t d\tau\, y(\tau).$$

As already mentioned in its definition, measuring the instantaneous frequency inherently involves a sampling or *gate time* τ. Thus, the result of measuring the instantaneous frequency can be expressed as the discretized derivate of the time deviation

$$\bar{y}(t) := \frac{x(t+\tau) - x(t)}{\tau}.$$

There is also another time constant due to some finite data processing time after sampling data, called the *dead time* τ_d. During this time, the measurement device is blind to the oscillator's signal, so information is lost. This can become a problem if $\tau \simeq \tau_d$.

Direct frequency counting is often not possible, especially if the oscillator has a nominal frequency in the optical regime, so indirect methods have to be used, several of which will be explained in later chapters.

- Mix the oscillator signal with a reference signal of comparable frequency and count the beat signal. See chapter 6 for an elaborate example.
- Phase-lock the reference to the test oscillator and observe the error signal. See chapter 1.2 for an introduction to phase-lock techniques.
- Electronically divide down the frequencies and then compare rise times with a high-resolution time interval counter.

These methods can be compared by what they can observe. The best method would be one that can measure the time deviation $x(t)$ directly, as changes in time, frequency and frequency changes could all be derived as numerical derivates of that data. On the other hand it is not possible to measure time deviations with a method that only observes frequency changes since there is always a dead time involved and numerical integration would produce erroneous data. Knowing this, the last method in the list

from above should theoretically be the best, were it not also the method fraught with the most technical noise issues. Counting rise times involves the use of digital counters for the frequency division which are inherently slower than analog methods based on observing beat notes.

What is the best measure of an oscillator's frequency instability? It needs to be a statistical estimator that is independent of the underlying noise spectrum. A lot of research has gone into looking at these estimators (see e.g. Allan *et al.* (1997) and Sullivan *et al.* (1990)), resulting in an internationally accepted standard for frequency instability called the *Allan variance*. It is defined as the time average of the square of fractional frequency deviations in the gate time interval $[t, t+\tau)$. Its square root is called the *Allan deviation* and is defined as:

$$\sigma_y(\tau) := \sqrt{\left\langle \frac{1}{2}(y(t+\tau) - y(t))^2 \right\rangle}. \tag{1.2}$$

Its best estimate from a sample of N fractional frequency measurements $\bar{y}_i$ is:

$$s_y(\tau) = \sqrt{\frac{1}{2(N-1)} \sum_{i=1}^{N-1} (\bar{y}_{i+1} - \bar{y}_i)^2}. \tag{1.3}$$

Although the Allan variance is independent of the underlying statistics, its error is not. The y_i are distributed differently for different kinds of noise processes (e.g. white frequency noise, $1/f$ phase noise, etc.) and the error depends on the noise process responsible for the distribution of frequency data. This makes it very difficult to handle, as one seemingly has to know the result of the measurement beforehand. Luckily, the error can be approximated as the error of an arithmetic mean with a noise process dependent prefactor (Lesage and Audoin, 1973, Sullivan *et al.*, 1990)

$$\Delta s_y(\tau) = \kappa_\alpha \frac{s_y(\tau)}{\sqrt{N-1}}$$

where κ_α is a scalar depending on the noise's spectral power law $S_\alpha(f) = \kappa_\alpha f^\alpha$. See Tbl. 1.1 for a list.

Plotting an imaginary oscillator's Allan deviation against the gate time τ in a log-log plot results in an intuitive estimate of the oscillator's instability. The lower part of

Noise process	α	κ_α
White phase noise	-2	0.75
Flicker phase noise	-1	0.77
White frequency noise	0	0.87
Flicker frequency noise	+1	0.99
Random walk frequency noise	+2	0.99

Table 1.1: Allan deviation errors for different noise processes (Sullivan *et al.*, 1990)

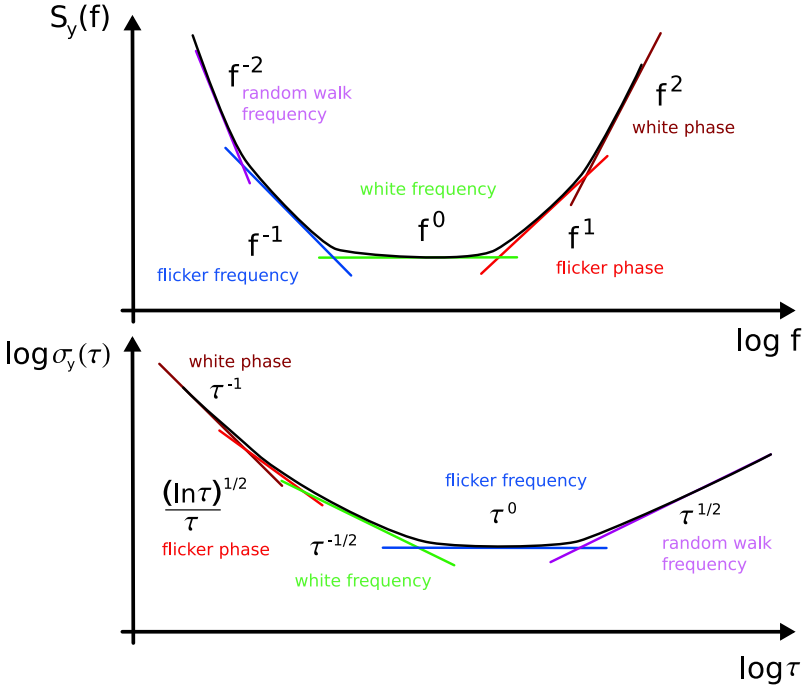

Figure 1.2: Noise power spectrum due to noise processes from Tbl. 1.1 and corresponding Allan deviation for a hypothetical oscillator.

Fig. 1.2 schematically shows the Allan deviation resulting from the noise spectrum in the upper part. Each noise source's spectral power law translates into a unique slope in the Allan deviation's logarithmic plot (Sullivan *et al.*, 1990). As long as the oscillator's error is dominated by statistical scatter around its nominal frequency, the Allan deviation averages down. At some point τ_0, random walk frequency noise takes over due to its $\tau^{1/2}$ dependence. Thus, if one wanted to use this hypothetical oscillator in an application, one would only trust it to remain stable on time scales shorter than τ_0.

1.2 Feedback theory and phase-locked loops

Copying of frequency and phase information from a frequency reference onto another oscillator is a very general and powerful tool used in almost any signal processing application. It allows synthesis of a frequency with well defined offset to the reference and also frequency multiplication by an adjustable factor. In the field of laser physics, synthesis of signals with highly stable frequency differences is of particular importance. Even more so, all electro-magnetic communication relies on the ability of every device to work in exactly the same frequency band, so every device must be referenced to a crystal oscillator.

A *phase-locked loop* (PLL) is a feedback loop working on any kind of *voltage-controlled oscillator* (VCO) . This VCO can be a pendulum driven by an electrical motor, an LC-

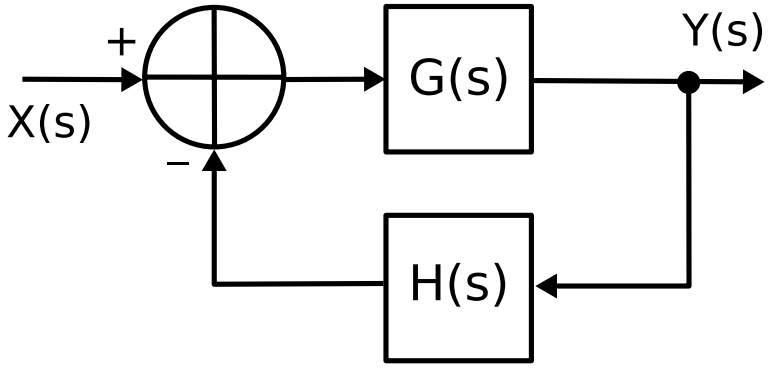

Figure 1.3: Negative feedback loop

circuit with a voltage controlled capacitance, a quartz crystal or even a laser whose oscillation frequency can be modified by changing a control voltage. The phase-locked loop tries to modify the control voltage in such a way that the emitted signal's frequency and phase match those of a reference signal, called the *local oscillator* (LO).

Note that every VCO has a characteristic time constant τ_0 and its output phase at time t is the integral over the control voltage from $t - \tau_0$ to t. This adds an implicit integration step to the feedback loop.

The next two Sections will introduce the general concepts of feedback theory and motivate why a PLL can be described in analogy to a classical feedback loop. The rest of this chapter explains the building blocks of a PLL in more detail.

1.2.1 Feedback theory

A feedback loop regulates an observable by measuring its current value and applying a control signal to the observable's source. They are ubiquitous in any technical application and there is a lot of theory surrounding the implementation details of feedback loops, such as stability and dynamic performance. We shall take a quick tour of the formalism needed to describe a negative-feedback loop.

Feedback loops are generally described by drawing a schematic like in Fig. 1.3 where the circuit implementing the loop is divided into different blocks. A *transfer function* (e.g. $G(s)$ in the upper part of the figure) is assigned to each block. This function describes how the block transforms an input signal X to an output signal Y. The output Y is fed back comparing it against the input: in our case with a negative sign to produce negative feedback (the comparator is depicted by a $\oplus$ in the diagram). In that manner, the whole feedback loop has a transfer function as well. There are some simple rules describing how to get the total transfer function from such a schematic[1]. One just multiplies each block's transfer function with the input to obtain the output signal and follows the path of the signal around the loop. In our case, this leads to the expression

$$Y = G(X - HY)$$

[1] A summary of *Mason's rules* can be found in Franklin *et al.* (1994).

which is an algebraic equation for the output Y as a function of the input X. We obtain

$$Y = \frac{G}{1+GH}X. \tag{1.4}$$

The nominator G is called the *forward gain*, the denominator is the *loop gain*. This equation allows the calculation of the output signal of the feedback loop for a given input signal in the following manner:

A transfer function can be assigned to any system that is described by a linear differential equation with constant coefficients of finite order. The time-dependent transfer function $G(t)$ is the Green's function of the system's differential equation, i.e. the response of the system to a kick. Any inhomogeneous solution can be found by convolving the Green's function with the inhomogeneity, viz. the input signal. However, this integration is difficult, so it is convenient to transform the problem to a simpler one by choosing an appropriate functional basis for the solution and work with the coefficients. It turns out that the most convenient basis consists of plane waves that are exponentially damped and cut off at time zero. This choice ensures convergence and causality of the solution and includes damped oscillatory behavior. The corresponding transformation is called one-sided Laplace transform which is a generalization of the Fourier transform to complex frequencies s:

$$F(s) = \int_0^\infty dt\, f(t)e^{-st} \tag{1.5}$$

$$f(t) = \frac{1}{2\pi i}\int_{\sigma-i\infty}^{\sigma+i\infty} ds\, F(s)e^{st} \tag{1.6}$$

with the complex integration path chosen to the right of all integrand poles.

As a generalization of the Fourier transform the Laplace transform also has the property of transforming convolutions in the time base to products in the frequency base. Since the system's output is a convolution between the Green's function and the input signal, evaluation of transfer functions in the new basis is very simple:

$$\begin{aligned} y(t) = G * x(t) &= \int_{-\infty}^{+\infty} d\tau\, G(t-\tau)x(\tau) \\ \Rightarrow Y(s) &= G(s)X(s) \end{aligned}$$

Once the output signal $Y(s)$ has been calculated, it can be transformed back into the time basis using Eq. 1.6. A table of transformation rules can be found in most books dealing with ordinary differential equations, e.g. Abramowitz and Stegun (1972). The transfer functions G and H are complex-valued. This leads to a special case when $\arg(GH) \approx \pi$. The denominator in Eq. 1.4 suddenly becomes large and the stabilizing effect of the negative feedback on the input signal disappears. Instead, the loop changes to positive feedback putting more energy into the system with every feedback cycle. If no safety guard against this effect is included, the output starts to oscillate wildly or even grows exponentially. The cause for this effect and a remedy by choosing appropriate forward gain will be shown in Sec. 1.2.4.

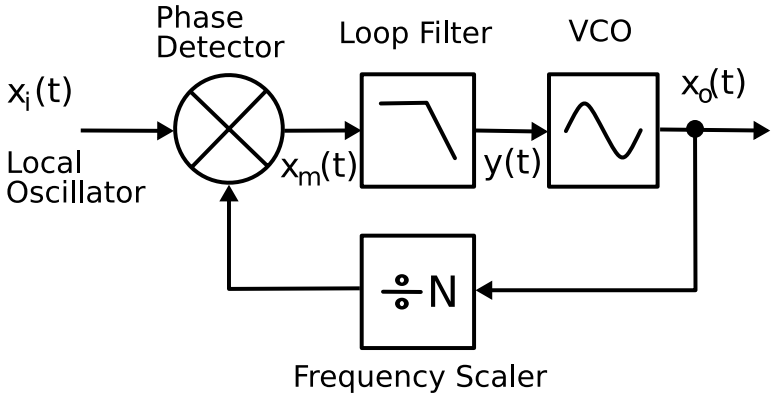

Figure 1.4: Schematic of a Phase-Locked Loop (PLL)

1.2.2 Application to phase-locked loops

Compare the basic setup of a PLL in Fig. 1.4 to then negative feedback loop in Fig. 1.3. The main difference is the multiplication of the analog mixer (depicted by $\otimes$) replacing the addition of signals. Remember that only linear systems can be treated with the methods introduced in the last Section. As mentioned before, this loop controls frequency by measuring phase. We will show that under certain approximations the linearity requirement is fulfilled and that the PLL behaves exactly like a standard feedback loop controlling the signal's phase.

The frequency division in the feedback arm is often used to compare a frequency divided signal to the reference, thus obtaining a phase-locked multiple of the input frequency at the output. In the following derivation, we will omit this division ratio, as it can easily be patched in once we have shown that the loop can be treated using a Laplace transform.

The circuit takes an input signal x_i from the LO and produces a sinusoidal signal x_o with phase θ_o. The mixer outputs the product of these signals

$$x_m(t) = x_i(t)x_o(t)$$

which is then fed into the loop filter. The loop filter modifies the signal so that it becomes a DC voltage able to drive the VCO:

$$y(t) = \int_0^\infty d\tau\, G_f(t-\tau)x_m(\tau)$$

Finally, the VCO converts an input voltage to a sine wave with amplitude a_o and phase $\theta_o + \pi/2$:

$$x_o(t) = a_o \sin(\theta_o(t) + \pi/2) = a_o \cos(\theta_o(t))$$
$$\theta_o(t) = \int_0^\infty d\tau\, G_v(t-\tau)y(t)$$

The transfer functions G_f and G_v of loop filter and mixer can be combined into a total forward gain transfer function by convolution: $G := G_f * G_v$. Combining the above equations we obtain a formal expression for the output phase:

$$\theta_o(t) = \int_0^\infty d\tau\, G(t-\tau) x_m(\tau)$$

Since we are interested in locking the VCO to a reference oscillator with a well-defined frequency, we will assume a sinusoidal input with amplitude a_i and phase θ_i

$$x_i(t) = a_i \sin\theta_i(t),$$

resulting in a mixed signal of the form

$$\begin{aligned} x_m &= a_i a_o \sin\theta_i \cos\theta_o \\ &= \frac{a_i a_o}{2}\left(\sin(\theta_i+\theta_o) + \sin(\theta_i-\theta_o)\right) \end{aligned}$$

Defining $a_m := a_i a_o/2$, the output phase reads:

$$\theta_o(t) = a_m \int_0^\infty d\tau\, G(t-\tau)\left(\sin(\theta_i+\theta_o) + \sin(\theta_i-\theta_o)\right). \tag{1.7}$$

The combined transfer function G includes the loop-filter and VCO characteristics. These electric parts include some RC combinations, maybe just due to residual capacitance and resistance of the components involved. The associated time constants will limit the system's memory and reduce the range of integral in Eq. 1.7 such that it will only need to be evaluated over an interval $[t-T, t]$ where T is the system's memory time.

This limitation to a finite interval allows us to approximate the sine terms under the integral. Let

$$\Omega_+(t) := \frac{d}{dt}(\theta_i+\theta_o)$$

be the instantaneous sum frequency and consider the sum frequency term

$$\int_{t-T}^{t} d\tau\, G(t-\tau)\sin(\theta_i+\theta_o).$$

If the sine function does many oscillations during the integration interval – corresponding to $T \gg 2\pi/\Omega_+$ – the integral will average to zero. Since the memory time can be set by choosing the loop filter variables, we will assume this to be true. We will also limit ourselves to the "locked" case where the output phase is already roughly equal to the input phase viz. $|\theta_i - \theta_o| \ll 1$. This allows us to linearize the difference frequency term and further simplify Eq. 1.7 to:

$$\theta_o(t) = a_m \int_{t-T}^{t} d\tau\, G(t-\tau)(\theta_i-\theta_o) \tag{1.8}$$

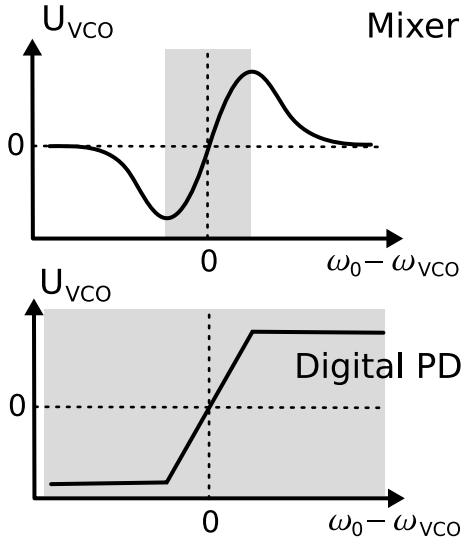

Figure 1.5: Analog and digital phase detector output signals and capture range

Formally extending the integration range to infinity by including the cutoffs in $G(t)$ allows us to simplify the expression even further: G in Eq. 1.8 is the Green's function of an ordinary differential equation with constant coefficients, so it can be solved using a Laplace transform as motivated in Sec. 1.2.1. The convolution of the transfer function with the input and output phases transforms into a product, leading to an algebraic equation for θ_o

$$\begin{aligned} \theta_o(s) &= a_m G(s)(\theta_i(s) - \theta_o(s)) \\ \Rightarrow \theta_o(s) &= \frac{a_m G(s)}{1 + a_m G(s)} \theta_i(s). \end{aligned}$$

In conclusion: the analog phase-locked loop is a classical feedback loop for the signal's phase if the input has a well-defined frequency, sufficient loop-filter integration is included and the phases of local oscillator and VCO are not too far apart.

1.2.3 Phase detector

As shown in the previous section, the mixer acts as a *phase detector* (PD) in a small range around $\omega_{\text{ref}} = \omega_v$, since the emitted signal can be approximated by a linear function in this region. If the VCO frequency is off by too much, the error signal from the mixer fluctuates too rapidly for the VCO to react, i.e. they happen on a faster time scale than the VCO's integration time.

The VCO averages these rapid oscillations to zero, as can be seen in the upper part of Fig. 1.5. That also means that an analog mixer is only useful in a small range around the target frequency: the loop does not know in which direction to regulate if the frequencies are too far apart. This limitation can be overcome by using a digital phase-detector that

rails to a constant voltage when not near the resonance. The phase detector becomes a *phase-frequency detector* (PFD) with a very large capture range (see lower part of Fig. 1.5), since the loop always knows in which direction to regulate the VCO frequency.

Note that there is a difference between a phase-locked loop's *capture range* – the frequency region where it is able to acquire lock – and its *bandwidth*, indicating its ability to follow rapidly changing input signals.

The downside of using a digital phase-frequency detector is that the logic circuitry is inherently slower than the analog mixer. This again amounts to an effective integration and limits the bandwidth of the feedback loop. In systems where high frequency noise is negligible, a digital phase-frequency detector is the preferred choice. This is true for most electronic circuits. However, if the feedback loop controls an optical oscillator like a laser diode, higher bandwidth might be necessary and an analog mixer should be used.

The bandwidth of a phase-locked loop can be measured by splitting off a fraction of the phase-detector's output and looking at its power spectrum on an FFT (Fast Fourier Transform) machine. By observing the difference between the noise floor of the locked and unlocked case, one gains a quantitative measure of how well the reference signal's characteristics are written onto the VCO output in a spectrally resolved manner. When the VCO is locked to the reference, the spectral power in the frequency range at which the feedback works should decrease compared to the unlocked case. This gives an estimate for the loop bandwidth.

As mentioned above, the bandwidth of a PLL is due to the amount of in-loop integration. Its main source is not the phase detector but the loop filter as will be explained in the next section.

1.2.4 Loop filter

The loop filter is responsible for adapting the error signal from the phase detector to match the VCO's needs. As shown in the preceding Sections it is important for the loop filter to low-pass filter the error signal. It is almost always true that the phase-detector's signal is much too weak to drive the VCO on its own, so the loop filter needs some sort of amplification as well. Luckily, it is very easy to implement active versions of RC combinations by using an operation amplifier. The loop filter transfer function becomes very important at this point; to talk about it further, we need a way to image this complex-valued function.

The complex transfer function $G(s)$ is usually depicted in a *Bode plot*, where amplitude (phase) is plotted against frequency on a log-log (log-linear) scale. The Bode plot for a passive RC low-pass is shown in Fig. 1.6(a). An active low-pass filter has the same Bode plot, but scaled by a gain factor (corresponding to adding a flat line to the Bode plot). Combining multiple transfer functions in a Bode plot is straightforward, as the product of the amplitudes is converted to a sum in the logarithmic plot and the arguments are added as well.

The combined transfer function of three low-pass filters with different time constants and some proportional gain is shown in Fig. 1.6(b). Note that the combined filter's transfer function has an amplitude that is much larger than unity at the point where

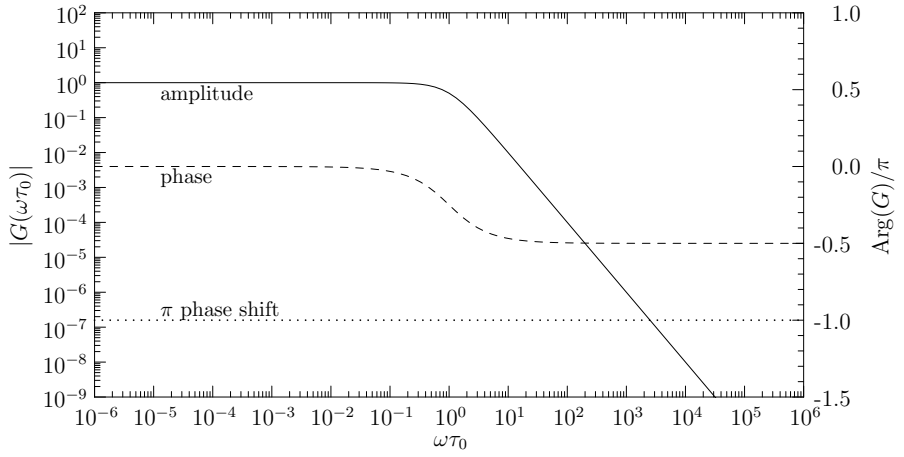

(a) One low-pass filter with unity gain.

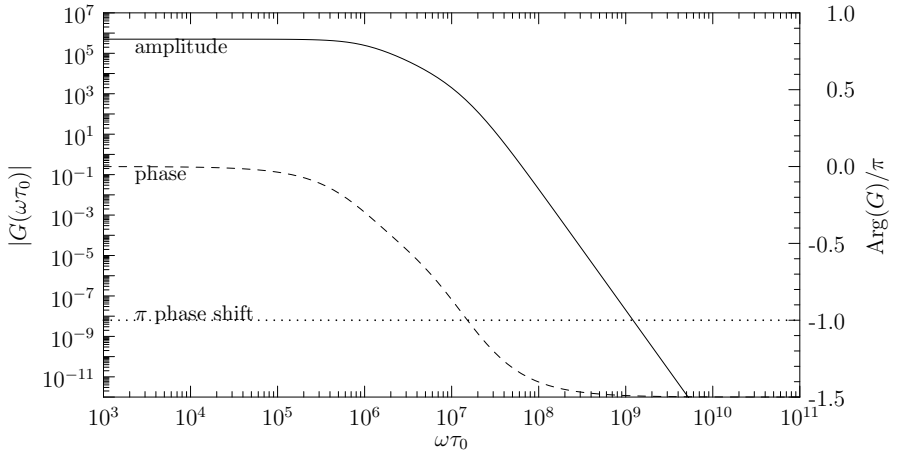

(b) Three low-pass filters in serial with large proportional gain at π-phase shift; this filter is unstable and will oscillate.

Figure 1.6: Bode representation for loop filter transfer functions

its phase-shift goes through $-\pi$. At this point, the negative feedback turns into positive feedback and the filter's output starts to oscillate. This loop filter must be redesigned so that it has a gain much less than unity at this point, i.e. $|G(\omega)| \ll 1$ for $\arg G(\omega) = -\pi$. The roll-off (the steepness of the gain's descent) and corner (the point where it starts to decrease) can be modified by altering or adding low-pass filters. See Franklin *et al.* (1994) for loop filter basics and Nash (1994) for a detailed manual on PLL loop filter design.

Chapter 2

Atomic Clocks and Precision Spectroscopy

An optical atomic clock is based on a transition between two specific states of a specific element. The element must be carefully chosen, subject to technical criteria.

The sample must produce a stable signal at a fixed frequency and should ideally only be limited by quantum mechanical measurement noise. To obtain such a clean signal, the environment of the sample must be controlled to an extreme extent: Ideally, the atoms should be as cold as possible to eliminate all temperature effects. The occurrence of the number of particles as $N^{-1/2}$ in the formula for the atomic clock's instability (Eq. 0.1) suggests that using many atoms to produce a signal might be beneficial. However, there is a trade-off between the extra noise introduced by many-body effects in the sample. At this time, these technical reasons point to two choices: Either use a few ions in an electro-magnetical trap or a few million neutral atoms inside an optical potential. Technical reasons make using ions attractive.

- The strong Coulomb interaction allows trapping ions in a very controlled environment provided by a Paul or Penney ion trap.
- The number of particles can be decreased to one, removing all many-body effects from the system.

On the other hand, neutral atoms have much smaller interaction strengths and allow using millions of particles without significant many-body effects. Finally, an experimental tool to trap neutral atoms is available with the optical lattice, allowing precision control comparable to the ion trap.

In this work, an all optical neutral atom based frequency standard for ^{87}Sr will be presented. This choice of sample was based on several considerations: Strontium is an alkaline earth, i.e. a two-electron system with a ground state configuration of (Kr $5s^2)^1S_0$. The two most abundant isotopes are ^{88}Sr (82.58(1) %) and ^{87}Sr (7.00(1) %). Due to the coupling between both valence electrons, the spectrum of two-electron systems is split into two parts: the singlet and the triplet states, corresponding to a total spin $S = 0$ or $S = 1$. Electronic dipole transitions between these subsystems (intercom-

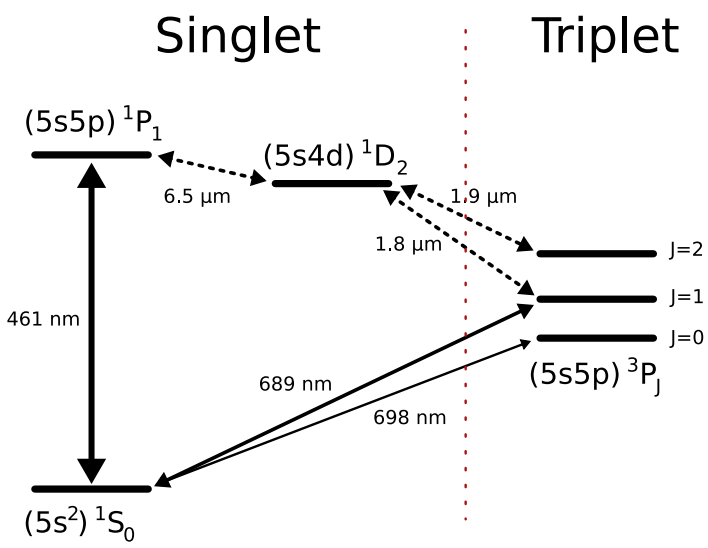

Figure 2.1: Lowest singlet and triplet states of neutral strontium

bination linens) are very unlikely and thus are called *forbidden*. A low probability for a dipole transition corresponds to a very narrow spectral line. The lowest electronic state manifold in the triplet system (^3P_J) can only decay to the lowest singlet state ($^1S_0$). For strontium a partial energy diagram is depicted in 2.1; the intercombination transition between $^1S_0$ and $^3P_1$ has a natural linewidth (wavelength) of 7.6 kHz (689 nm). The broad $^1S_0 - {}^1P_1$ transition (32 MHz, 461 nm) lends itself to standard MOT cooling into the mK regime (as will be discussed in the next chapter). The spectrum of both isotopes is almost identical, except that ^{88}Sr and ^{87}Sr have different nuclear spin. Whereas ^{88}Sr has no nuclear spin ($I = 0$) and thus no hyperfine structure, ^{87}Sr has $I = 9/2$ leading to fine but interesting differences.

The hyperfine interaction makes the doubly forbidden $^1S_0 - {}^3P_0$ transition[1] weakly allowed by adding some $^1P_1$ character to the $^3P_1$ state and perturbing $^3P_0$ (see Sec. 4.6.4). The transition has a theoretical linewidth of 8 mHz (Porsev and Derevianko, 2004). Characterizing this extremely narrow transition is the first step towards an all optical lattice based frequency standard with instability on the 10^{-18} level.

The next two chapters will discuss the preparation of these strontium atoms, viz. we shall talk about laser cooling and trapping of neutral atoms.

[1] Doubly forbidden because of $\Delta S = 1$ and $\Delta J = 0$.

Chapter 3

Doppler Cooling and Magneto-Optical Traps

The basics of laser cooling neutral atoms are introduced, leading to a discussion of narrow-line MOTs for alkaline earths.

3.1 Doppler cooling

Laser cooling of atoms relies on the mechanical effects of the photon-atom interaction. Due to momentum conservation, absorption (emission) of a photon with momentum $\hbar\boldsymbol{k}$ forces the particle to increase (decrease) its own momentum by the same amount. Light acts on matter in another distinctive way: the electric field of the photon causes an intensity dependent shift of the atom's electronic spectrum, called the *AC-Stark shift*. These mechanical light effects have been studied extensively and allow a plethora of schemes to influence an atomic sample's phase space distribution. I will give a brief overview and direct the reader to Stenholm (1986), Adams and Riis (1997) or Metcalf and van der Straten (1999) for more in-depth information.

The dynamics of laser cooling can be described in a semi-classical way by the *Fokker-Planck equation*[1]. It describes the evolution of an atomic ensemble's momentum distribution W and includes two modifying terms: a dissipation term $\boldsymbol{F}$ that removes amplitude from the distribution and a redistributing diffusion term D, viz.

$$\partial_t W(\boldsymbol{p},t) = -\nabla \boldsymbol{F}(\boldsymbol{p},t)W(\boldsymbol{p},t) + \triangle D(\boldsymbol{p},t)W(\boldsymbol{p},t) \tag{3.1}$$

The dissipative function $\boldsymbol{F}$ "decelerates" particles of momentum $\boldsymbol{p}$ and the diffusive function D "spreads" them to different momenta. In the case of laser cooling, these momentum-changing effects are the absorption and spontaneous emission of a photon and the atom's corresponding momentum change. Deceleration can be achieved by providing a preferred direction for the absorption of photons, e.g. a laser beam with wave vector $\boldsymbol{k}$, whereas diffusion is due to the randomness in the direction of spontaneous emission.

[1] See Risken (1996) and Gardiner (2004).

3.1.1 Dissipative force

The simplest velocity-dependent force that can be used for laser cooling is provided by the *Doppler effect* which moves atomic transitions in or out of resonance according to the atom's velocity vector. The atom's absorption probability becomes velocity dependent and so does the net force exerted through absorption processes (assuming a two-level system with states $|g\rangle$,$|e\rangle$):

$$\boldsymbol{F} = \hbar \boldsymbol{k} \gamma \rho_{ee}$$

where γ is the Einstein A coefficient of the transition and ρ_{ee} is the excited state population (the corresponding diagonal element of the system's density matrix). Calculating a steady-state solution for the two-level system lends

$$\rho_{ee}(t) = \frac{s_0/2}{1 + s_0 + (2\Delta/\gamma)^2)}$$

where the *saturation parameter* $s_0 \in [0, 1]$ is the ratio between the laser intensity I and the *saturation intensity* I_s that would equally distribute population between both levels. The parameter Δ is the *detuning* between the transition frequency and the laser frequency. The detuning is modified by the atom's velocity $\boldsymbol{v}$ due to the Doppler effect:

$$\Delta = \delta - \boldsymbol{k} \cdot \boldsymbol{v}.$$

Putting all of the above together, we obtain an expression for the velocity-dependent dissipative force $\boldsymbol{F}$

$$\boldsymbol{F}(\boldsymbol{v}) = \hbar \boldsymbol{k} \gamma \frac{s_0/2}{1 + s_0 + \left(\frac{2}{\gamma}(\delta - \boldsymbol{k} \cdot \boldsymbol{v})\right)^2}.$$

Assuming that the Doppler effect is small compared to the detuning δ, i.e. $\frac{\boldsymbol{k} \cdot \langle \boldsymbol{v} \rangle}{\delta} \ll 1$, this expression can be expanded and approximated as

$$\boldsymbol{F}(\boldsymbol{v}) \simeq \boldsymbol{F}_0 - \beta \boldsymbol{v}$$

with friction coefficient

$$\beta := -4\hbar k^2 \frac{s_0 \delta/\gamma}{(1 + s_0 + (2\delta/\gamma)^2)^2}. \tag{3.2}$$

Note that $\delta = \omega_{eg} - \omega_l < 0$ for a red-detuned laser and that δ is the only quantity determining the sign of the friction force. Correspondingly, a blue-detuned laser will heat up the ensemble.

3.1.2 Diffusion rate

The diffusion function D is calculated by approximating it as its value at $p = 0$, which can be obtained in a treatment analogously to Brownian motion – see Stenholm (1986). This leads to an expression for $D(p, t) \equiv D_0$

$$2D_0 t = \hbar^2 k^2 (1 + Q + \xi) R t$$

which is the sum of three different contributions, where $R = \gamma\rho_{ee}$ is the scattering rate from above. The first summand is due to absorption and subsequent emission of a photon, the second term contains the *Mandel Q-parameter*

$$Q = \frac{\langle \Delta n^2 \rangle - \langle n \rangle}{\langle n \rangle}$$

that describes the deviation of photon statistics from the Poissonian case. For typical laser light, this is a small parameter and can be omitted. The last term contains ξ, a geometric factor for the angular distribution of spontaneous emission. We obtain

$$D_0 = \hbar^2 k^2 \gamma \frac{1+\xi}{2} \frac{s_0/2}{1 + s_0 + (2\delta/\gamma)^2}, \tag{3.3}$$

which is a non-negative quantity. Thus, diffusion is always outwards and can never shrink the momentum distribution.

3.1.3 Cooling limits

Ultimately, every laser cooling scheme relying solely on spontaneous emission for energy dissipation will be limited by the transition's energy uncertainty γ, resulting in an absolute lower limit of $k_B T = \hbar\gamma$.

In the present case, the cooling is actually already limited by the counterplay of the two processes discussed above: dissipation cools the ensemble, diffusion heats it up. The limiting temperature – called the *Doppler temperature* T_D – is determined by the ratio of both processes, represented by the friction (Eq. 3.2) and diffusion (Eq. 3.3) coefficients:

$$k_B T_D = \frac{D_0}{\beta} = -\frac{1+\xi}{8} \hbar\gamma \frac{1 + s_0 + (2\delta/\gamma)^2}{\delta/\gamma} \tag{3.4}$$

3.2 Magneto-optical traps

An important improvement on the simple Doppler cooling scheme from the previous Section is the *Magneto-Optical Trap* (MOT). It combines optical cooling with an inhomogeneous magnetic field designed to make use of magnetic sublevels. It not only cools the ensemble, but also confines it spatially.

Two counter-propagating laser beams with different circular polarization $\sigma^{\pm}$ cool atoms on a $J = 0 \rightarrow J = 1$ transition. Additionally a magnetic field $B = az$ is applied along the laser axis that splits the magnetic sublevels of the excited state as depicted in Fig. 3.1. This Zeeman splitting is added to the Doppler shift in determining the force acting on the atoms from each beam:

$$\boldsymbol{F}^{\pm} = \pm\hbar\boldsymbol{k}\gamma \frac{s_0/2}{1 + s_0 + (2\delta^{\pm}/\gamma)^2}$$

with the space and velocity dependent detuning $\delta^{\pm}$

$$\delta^{\pm} = \delta \mp \boldsymbol{k} \cdot \boldsymbol{v} \mp \mu' B/\hbar,$$

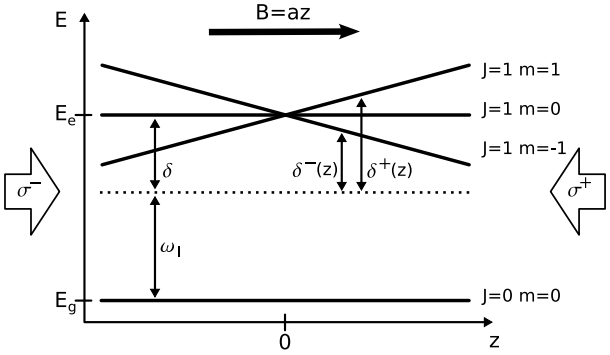

Figure 3.1: MOT detunings

where $\mu' = (g_e m_e - g_g m_g)\mu_B$ is the transition's *effective magnetic moment*, assuming σ^+-polarized laser light. Adding both forces and expanding again for small Doppler shift and Zeeman splitting cancels the common zeroth order term resulting in

$$\boldsymbol{F} = \boldsymbol{F}^+ + \boldsymbol{F}^- \simeq -\beta \boldsymbol{v} - \kappa \boldsymbol{r}$$

with β defined as in Eq. 3.2 and a spring constant

$$\kappa = \frac{\mu' a}{\hbar k}\beta.$$

More generally, a MOT will work for any $J \rightarrow J+1$ transition as long as the g-factors of both states are approximately equal. The Zeeman splitting of all magnetic sublevels will be matched and all transitions happen at the same frequency. Note that the Clebsch-Gordan coefficients for $\sigma^+(\sigma^-)$ transitions increase monotonically towards the largest (smallest) magnetic quantum number, optically pumping population towards the outer magnetic sublevels.

In the case that the g-factors and thus the magnetic splitting of both electronic states are very disparate, the exciting laser beams cannot drive every $m \rightarrow m \pm 1$ transition with the same efficiency. The transition frequency $\omega_{eg}(x)$ for the σ^+ beam is (assuming $g_e \gg g_g$ without loss of generality)

$$\begin{aligned}\hbar\omega_{eg}(x) &= \hbar\omega_0 + \mu' B(x) \\ &= \hbar\omega_0 + \mu_B(m_e g_e - m_g g_g)B(x) \\ &\simeq \hbar\omega_0 + \mu_B m_e g_e a x.\end{aligned}$$

which is completely determined by the state with the larger g-factor.

The MOT will still work if the transition is broad enough, such that the exciting laser can still reach the magnetic sublevels with small Clebsch-Gordan coefficients without losing trapped atoms due to photon recoil. This results in a limiting case, where the electronic transition's width γ is smaller than the recoil frequency $\varepsilon_r/\hbar$, such that the absorption of a single photon removes an atom from the trap.

By simulating the optical pumping happening in a broad-line MOT, the efficiency of a narrow-line MOT can be significantly improved, as demonstrated by Mukaiyama *et al.* (2003). This so-called *Dynamic MOT* (DMOT) statistically mixes magnetic sublevels by coupling the lower electronic state to another one with comparable g-factor via a "stirring" laser. Rapid Rabi oscillations on the stirring transition shuffle population between the magnetic sublevels. The population of the trapped state is stochastically amplified, improving the trapping time by a factor of 6.

Chapter 4

1D Optical Lattices

Neutral atoms can be trapped using an optical potential called *optical lattice*. The spatial intensity variation of a standing wave formed by two counter-propagating laser beams of equal intensity and polarization produces a trap due to the AC Stark effect.

Optical lattices have become one of the standard tool to trap neutral atoms over the last decade due to the simplicity and controllability provided by this all-optical atomic trap. This Chapter provides a detailed introduction to one-dimensional (1D) optical lattices, their motional structure and effect on precision spectroscopy of narrow optical transitions. First, we need to understand the cause of the trapping force: the AC Stark effect.

4.1 AC Stark effect

The AC Stark shift of level i is the second order perturbation of the atomic spectrum caused by an electric field $\boldsymbol{E}$ in the dipole approximation (as derived in e.g. Merzbacher, 1998) and is given by:

$$\Delta E_i = -\frac{1}{2}\alpha|\boldsymbol{E}|^2$$

where α is the polarizability of the state $|i\rangle$. The dynamic dipole polarizability for an exciting plane wave with electric field $\boldsymbol{E} = \mathcal{E}\hat{\boldsymbol{z}}$ and frequency ω caused by the presence of other states $|f\rangle$ as defined in Bransden and Joachain (2003) is

$$\alpha_i(\omega) = \frac{2e^2}{\hbar}\sum_{f\neq i}\omega_{fi}\frac{|\langle f|z|i\rangle|^2}{\omega_{fi}^2-\omega^2},$$

with $\hbar\omega_{fi} := E_f - E_i$. The dipole moment $z_{fi} := \langle f|z|i\rangle$ can be expressed in terms of the transition's Einstein A coefficient (see e.g. Loudon, 1983)

$$A_{fi} = \frac{e^2\omega_{fi}^3}{3\pi\epsilon_0\hbar c^3}|z_{fi}|^2.$$

We obtain

$$\alpha_i(\omega) = 6\pi\epsilon_0 c^3 \sum_{f\neq i} \frac{A_{fi}}{\omega_{fi}^2(\omega_{fi}^2 - \omega^2)}.$$

The static polarizability α_i^s is the limit for infinite wavelength, i.e.

$$\alpha_i^s = \lim_{\omega\to 0} \alpha_i(\omega) = 6\pi\epsilon_0 c^3 \sum_{f\neq i} \frac{A_{fi}}{\omega_{fi}^4}.$$

The Einstein A coefficients for each particular transition are usually not available in the literature. Instead, total lifetimes are given. This is not a big problem, though, as the fraction of the lifetime due to decay to a certain level can be calculated. These fractions are called branching ratios and will be discussed in the next section.

4.1.1 Branching ratios

Branching ratios can be obtained by using the Wigner-Eckart theorem, which allows separation of matrix elements of tensor operators (See e.g. Sakurai, 1994, Ch. 3). Applying the theorem to the present case while ignoring hyperfine structure, we can obtain the matrix elements of the dipole operator $\boldsymbol{D}_q$ for light with polarization quantum number q in terms of geometric factors (Clebsch-Gordan coefficients) and reduced matrix elements:

$$\langle J_f m_f|\boldsymbol{D}_q|J_i m_i\rangle = \langle J_f m_f|1 J_i q m_i\rangle\langle J_f\|\boldsymbol{D}\|J_i\rangle$$

$$\langle J_f\|\boldsymbol{D}\|J_i\rangle := \delta_{S_f S_i}(-1)^{1+S_f+J_i+L_f}\sqrt{2J_i+1}\sqrt{2L_f+1}\begin{Bmatrix} J_f & J_i & 1 \\ L_i & L_f & S_i\end{Bmatrix}\langle L_f\|\boldsymbol{D}\|L_i\rangle$$

where the expression in curly braces is a *6j-symbol*[1], a group-theoretic factor. The Clebsch-Gordan coefficients enforce the selection rule $m_f = m_i + q$. Since the angular momentum is a composite of the angular momenta of two electrons, the corresponding selection rule is $L_f = L_i, L_i \pm 1$.

These expressions are very useful since the Einstein A coefficients for a transition are proportional to the square of the dipole operator's matrix elements. Suppose we have been given a total inverse lifetime $A(SLJ)$ for a certain ${}^{2S+1}L_J$ state and we want to know how much of this width is due to decay to ${}^{2S+1}L'_{J'}$. An expression for the total decay rate $A(SLJ)$ can be found by summing over the matrix elements above

$$\begin{aligned} A(SL_iJ_i) \propto & \sum_{L_f=|L_i\pm 1|}^{L_f+S} \sum_{J_f=|L_f-S|}^{+J_f} \sum_{m_f=-J_f}^{+J_i} \sum_{m_i=-J_i}^{+1} \sum_{q=-1} |\langle J_f m_f|1 J_i q m_i\rangle|^2 \times \\ & \times (2J_i+1)(2L_f+1)\begin{Bmatrix} J_f & J_i & 1 \\ L_i & L_f & S\end{Bmatrix}^2 |\langle L_f\|\boldsymbol{D}\|L_i\rangle|^2 \\ \equiv & \sum_{L_f=|L_i\pm 1|}^{L_f+S} \sum_{J_f=|L_f-S|} A(SL_iJ_i \to SL_fJ_f) \end{aligned}$$

[1] Included in Mathematica as the `SixJSymbol` function. See Brink and Satchler (1968) and Rotenberg *et al.* (1959) for detailed information.

Using an orthogonality relation for Clebsch-Gordan coefficients

$$\sum_{m_1 m_2} \langle j_1 j_2 m_1 m_2 | j m \rangle \langle j_1 j_2 m_1 m_2 | j' m' \rangle = \delta_{jj'} \delta_{mm'},$$

and noting that $\sum_{m_f} 1 = 2J_f + 1$, we can simplify the above to

$$A(SL_i J_i \to SL_f J_f) = (2J_f + 1)(2J_i + 1)(2L_f + 1) \begin{Bmatrix} J_f & J_i & 1 \\ L_i & L_f & S \end{Bmatrix}^2 |\langle L_f \| \boldsymbol{D} \| L_i \rangle|^2.$$

By dividing through the known total line width this expression lends the branching ratio

$$\frac{A(SL_i J_i \to SL_f J_f)}{A(SL_i J_i)} = (2J_f + 1)(2L_f + 1) \begin{Bmatrix} J_f & J_i & 1 \\ L_i & L_f & S \end{Bmatrix}^2 |\langle L_f \| \boldsymbol{D} \| L_i \rangle|^2.$$

The reduced matrix element involving the composite angular momenta L_f and L_i depends on the decomposed angular momenta involved. Evaluating this reduced matrix element requires knowledge of the underlying many-body wave function, as shown in Brink and Satchler (1968, p. 83-85). We will approximate it as constant for all involved combinations of L_i and L_f, justifying this approximation by only considering small values of L: The reduced matrix element is a linear combination of radial integrals which will vary very little except in the case of large wavefunctions (large principal quantum number) and large values of L (many nodes), i.e. Rydberg states. In this approximation, the branching ratio becomes a geometric factor that can be evaluated easily:

$$\frac{A(SL_i J_i \to SL_f J_f)}{A(SL_i J_i)} \approx (2J_f + 1)(2L_f + 1) \begin{Bmatrix} J_f & J_i & 1 \\ L_i & L_f & S \end{Bmatrix}^2.$$

4.1.2 Introducing experimental parameters

Finally, we express the laser's electric field in terms of experimental parameters. We can write the field as a superposition of two counterpropagating Gaussian beams in cylindrical coordinates. We assume that the lattice is formed by one beam only (with polarization vector $\hat{\boldsymbol{\varepsilon}}_+$) which is reflected back onto itself with a curved mirror with intensity loss $\eta \ll 1$ that also rotates the polarization to $\hat{\boldsymbol{\varepsilon}}_-$:

$$\boldsymbol{E}(r, z) = \mathcal{E} e^{-\frac{r^2}{w(z)^2}} \left(\hat{\boldsymbol{\varepsilon}}_+ e^{-i\kappa z} + \hat{\boldsymbol{\varepsilon}}_- \sqrt{1 - \eta}\, e^{i\kappa z} \right)$$

The AC Stark shift is

$$\begin{aligned} \Delta E(r, z) &= -\frac{1}{2} \alpha |\boldsymbol{E}|^2 \\ &= -\frac{1}{2} \alpha \mathcal{E}^2 e^{-\frac{2r^2}{w(z)^2}} \left| \hat{\boldsymbol{\varepsilon}}_+ e^{-i\kappa z} + \hat{\boldsymbol{\varepsilon}}_- \sqrt{1 - \eta}\, e^{+i\kappa z} \right|^2 \\ &= -\frac{1}{2} \alpha \mathcal{E}^2 e^{-\frac{2r^2}{w(z)^2}} 2 \left[1 - \frac{\eta}{2} + \sqrt{1 - \eta} \cos(\hat{\boldsymbol{\varepsilon}}_+, \hat{\boldsymbol{\varepsilon}}_-) \cos 2\kappa z \right], \end{aligned}$$

resulting in

$$\Delta E(r,z) = -\frac{1}{2}\alpha\mathcal{E}^2 e^{-\frac{2r^2}{w(z)^2}} 4\cos^2\kappa z$$

for perfectly parallel polarization and full reflection. In the imperfect case, the trap depth is reduced and for non-zero η, the energy origin is shifted. For the present discussion, we will limit ourselves to the ideal case. The maximal electric field amplitude $\mathcal{E}$ can be expressed in terms of the laser power P by using the maximal intensity

$$I_{\max} = \frac{1}{2}\epsilon_0 c\mathcal{E}^2 = \frac{P}{\pi w_0^2}.$$

We find that the optical lattice potential for state $|i\rangle$ is

$$\Delta E_i(\omega) = -\frac{4P}{\pi\epsilon_0 c w_0^2}\alpha_i(\omega) e^{-\frac{2r^2}{w(z)^2}} \cos^2\kappa z. \tag{4.1}$$

4.2 Separating the motion

The AC Stark shift depends on the electronic state of the atom. This becomes a problem in experiments involving other electronic states, e.g. when doing Rabi oscillations between two levels. The excited state will experience a different AC Stark shift and might not even be trapped at all. One would like to separate the motional degrees of freedom from the electronic excitation to be able to describe the system as a tensor product between the motional and electronic state spaces. The quantity responsible for the different behavior of different electronic states is the dynamic polarizability as defined in the last section. Since the polarizability is frequency-dependent, it is possible in some cases to find a *magic wavelength* where the AC Stark shifts of both levels are matched (Kimble *et al.*, 1999). To decide whether this is possible for a particular combination of states, one has to calculate the dynamic polarizabilities and plot them as function of wavelength. For the case of ^{87}Sr, a scheme using a magic wavelength has been proposed by Katori (2002); the polarizabilities and numerical values will be presented in Sec. 4.6.2.

For now, let us assume that we can separate the motional degrees of freedom from the electronic states and try to find a quantum mechanical description of the lattice potential. However, it quickly turns out that the motional potential in Eq. 4.1 is not separable: it is a product of the transversal (Gaussian) and longitudinal (sinusoidal) confinement.

As a first approximation, we will ignore the transversal degrees of freedom and try to solve the longitudinal problem. This will provide us with the lattice band structure and wave functions and allow us to estimate the effect of laser intensity noise or vibrating optical elements.

4.3 Longitudinal problem

The one-dimensional optical lattice has traditionally been treated by approximating the potential at each site by an harmonic oscillator. For shallow lattices, the anharmonicity

of the potential starts to modify the system's dynamics drastically[2].

Setting $r = 0$ in Eq. 4.1, we ignore the Gaussian part for the moment and solve the 1D Schrödinger equation for the potential (renaming the variable z to x for the remainder of this section)

$$V(x) = 4V_{\max}\cos^2(\kappa x)$$

Requiring translation invariance in the solution, the time-independent Schrödinger equation becomes

$$\begin{aligned} Hu_k(x) &= \left[\frac{1}{2m}\left(\frac{\hbar}{i}\frac{d}{dx} + \hbar k\right)^2 + V(x)\right] u_k(x) \\ &= \varepsilon u_k(x) \end{aligned}$$

Using a modulated plane wave ansatz

$$u_k(x) = \varphi(x)e^{-ikx}$$

and the dimensionless variable $\xi := \kappa x$ we obtain an equation for $\varphi(\xi)$:

$$\varphi'' + (a - 2q\cos 2\xi)\varphi = 0 \tag{4.2}$$

with parameters

$$q = \frac{V_{\max}}{\varepsilon_r}, a = \frac{\varepsilon}{\varepsilon_r} - 2q$$

and lattice recoil energy

$$\varepsilon_r = \frac{2\pi^2\hbar^2}{m\lambda^2}$$

This equation is known as *Mathieu's differential equation* and also describes the motion of a particle in an ion trap or a quadrupole mass filter.

Mathieu's equation has stable solutions only for certain combinations of the a and q parameters. Since q is the potential height in recoil units and $a + 2q$ is the particle's energy, plotting $a(q)$ gives a list of allowed energy ranges: the band structure of the one-dimensional optical lattice.

Finding the eigenfunctions requires a detour into the theory of ordinary differential equations with periodic coefficients. See Abramowitz and Stegun (1972) for more information and Heuser (1995) for a more general version of the theorem.

Theorem (Floquet's theorem). *The differential equation $y'' + Q(x)y = 0$ with a piecewise continuous and periodic coefficient $Q(x)$ of period π, i.e. $Q(x+\pi) = Q(x)$, has two continuously differentiable solutions $y_\pm(x) = e^{\pm i\nu x}P_\nu(\pm x)$ where P_ν is also periodic with period π.*

[2] After having developed the 1D lattice theory presented in this Chapter, it was pointed out to me that there already are several papers based on the same ideas and sources (Jáuregui *et al.*, 2001, Jáuregui, 2001, Poli *et al.*, 2002). The theory presented here still is a bit more general, due to using the problem's real eigenfunctions.

This can be directly applied to our case, i.e. the Mathieu equation Eq. 4.2 has two Floquet solutions

$$F_\nu^\pm(\xi) = e^{\pm i\nu\xi} P_\nu(\pm\xi)$$

which are linearly independent for non-integer ν. The parameter ν (called the solution's *characteristic exponent*) indexes the wave function's energy eigenvalue, that is its position in the band structure. Note that $F_\nu^\pm$ is generally not π-periodic, but the Bloch wave function $u_k(\xi)$ must be. It follows that there must exist a relation between the wave number k and the characteristic exponent ν. By requiring

$$u_k(\xi + \pi) = u_k(\xi)$$

we find for the n-th band, that there must exist numbers $p \in \mathbb{Z}$ and $r \in [0, 1)$ such that

$$\begin{aligned} p + r &= k/\kappa \\ \nu &= n + r. \end{aligned}$$

Thus the forward and backward "plane waves" of the 1D lattice corresponding to the two Floquet solutions read

$$u_{k,n}^\pm(\xi) = e^{\mp ip\xi} e^{\pm in\xi} P_{n+r}(\pm\xi).$$

Here n indexes the band and $r = k/\kappa - \lfloor k/\kappa \rfloor$ determines the intra-band position corresponding to a certain quasi-momentum k (the half brackets indicate rounding down to the next integer). Since the Bloch wave function is periodic in the lattice, a phase factor $e^{\mp ip\xi}$ with integer $p = \lfloor k/\kappa \rfloor$ represents the same physical situation.

We are interested in localized particles in a finite lattice and want to construct a localized *Wannier basis* for this problem, i.e. a basis of site- and band-orthonormal wave functions. The Wannier functions must conform to

$$\langle i, n | j, m \rangle = \delta_{ij}\delta_{nm}.$$

This can be achieved by building superpositions of Bloch waves of the same band n in such a way that the i-th Brillouin zone of the lattice becomes their support. The most general superposition of this kind looks like

$$w_n^i(\xi) := \sum_{p\in\mathbb{Z}} e^{-ip\xi} \int_0^1 dr\, \alpha_{np}^i(r) e^{in\xi} P_{n+r}(\xi) + \sum_{p\in\mathbb{Z}} e^{ip\xi} \int_0^1 dr\, \beta_{np}^i(r) e^{-in\xi} P_{n+r}(-\xi)$$

Note that the Floquet solution only exists for rational $n + r$, so the integral needs to be evaluated in $\mathbb{Q}$. In practice, this is not a problem as numerical integration uses floating point numbers of finite precision, i.e. rational numbers.

To simplify this expression, we will look at the lower lattice bands that lend themselves to localization, viz. the bands are narrow and look like discrete levels (true for $n \ll \sqrt{q}$). As the Floquet solutions are continuously dependent on the parameter ν between

integral values, in this case they do not vary much over the whole range of r and we can approximate

$$P_{n+r}(\pm\xi) \simeq P_n(\pm\xi),$$

leading to

$$w_n^i(\xi) \simeq e^{in\xi} P_n(\xi) \sum_{p\in\mathbb{Z}} e^{-ip\xi} \int_0^1 dr\, \alpha_{np}^i(r) + e^{-in\xi} P_n(-\xi) \sum_{p\in\mathbb{Z}} e^{ip\xi} \int_0^1 dr\, \beta_{np}^i(r).$$

We choose superposition coefficients α, β such that

$$\sum_{p\in\mathbb{Z}} e^{-ip\xi} \int_0^1 dr\, \alpha_{np}^i(r) = \sum_{p\in\mathbb{Z}} e^{ip\xi} \int_0^1 dr\, \beta_{np}^i(r) =: c_n^i \Theta_i(\xi)$$

with the supporting function of the i-th Brillouin zone

$$\Theta_i(\xi) = \begin{cases} 1 & \xi \in [i\pi, (i+1)\pi) \\ 0 & \text{else} \end{cases}$$

and normalization constants c_n^i. The Wannier function becomes

$$\begin{aligned} w_n^i(\xi) &= c_n^i \Theta_i(\xi) \left[e^{in\xi} P_n(\xi) + e^{-in\xi} P_n(-\xi) \right] \\ &= 2c_n^i \Theta_i(\xi)\, \mathrm{ce}_n(\xi) \end{aligned}$$

where $\mathrm{ce}_n(\xi)$ is the n-th even Mathieu function as tabulated in Abramowitz and Stegun (1972). Note that these functions are again π-periodic and form a complete orthogonal set on $[0, \pi]$. Also note that ce_n has no closed form and has to be evaluated numerically as pointed out by Jáuregui *et al.* (2001), but that it is implemented in e.g. Mathematica as the `MathieuC` function. The normalization constants are evaluated by calculating (see Abramowitz and Stegun, 1972, p. 732)

$$\begin{aligned} \|w_n^i\|^2 &= |2c_n^i|^2 \int_{\Theta_i} d\xi\, |\,\mathrm{ce}_n(\xi)|^2 \\ &= |2c_n^i|^2 \int_0^\pi d\xi\, |\,\mathrm{ce}_n(\xi)|^2 \\ &= |2c_n^i|^2 \frac{\pi}{2} \\ &\Rightarrow 2c_n^i = \sqrt{\frac{2}{\pi}} \end{aligned}$$

To summarize: the localized wave functions used in this paper are

$$w_n^i(\xi) = \sqrt{\frac{2}{\pi}} \Theta_i(\xi)\, \mathrm{ce}_n(\xi).$$

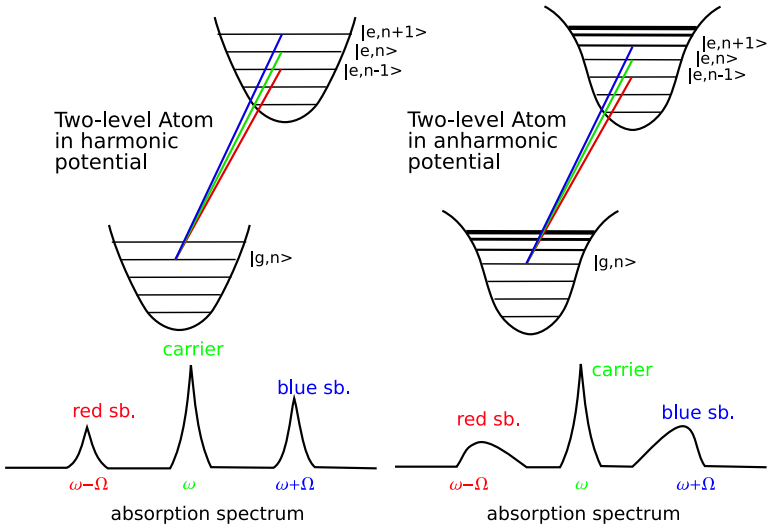

Figure 4.1: Motional sidebands in harmonic and anharmonic potentials

4.4 Vibrational spectroscopy

The motional structure derived in the last section can be probed using high-resolution laser spectroscopy. Recall that we were able to separate the motional degrees of freedom from the electronic states by matching the AC Stark shifts. In analogy to ion trapping experiments, where ions are electromagnetically trapped in a harmonic potential, there exists a regime where the vibration of particles around their rest position can be observed by taking a spectral scan of the electronic transition.

This regime is known as the *Lamb-Dicke regime* and requires an exciting laser beam that probes the electronic transition $|g\rangle \rightarrow |e\rangle$ at ω_{eg}. If its wavelength λ is much larger than the typical excursion x_0 of the trapped particles, corresponding to a *Lamb-Dicke parameter* $\eta := \frac{2\pi}{\lambda} x_0 \ll 1$, and the electronic transition is sufficiently narrow, i.e. its linewidth γ is less than the vibration frequency Ω, the atomic motion produces sidebands on the electronic carrier transition. The lowest order sidebands are detuned by $\pm\Omega$ from ω_{eg}.

To understand the sideband shape, one has to take a closer look at their origin. Fig. 4.1 is a cartoon of a system where the m-th sideband is composed of all inelastic transitions from the electronic ground state and n-th motional state $|g, n\rangle$ to the electronically excited state and modified motional state $|e, n + m\rangle$. The left hand side depicts an harmonic potential (e.g. an ion trap), where these inelastic transitions have exactly the same transition frequency and all the contributions add up to a Lorentzian line shape, because the harmonic trapping spaces the motional states uniformly. This is different in an optical lattice (as shown on the right hand side of Fig. 4.1): the potential formed by the light shift of a standing wave is sinusoidal resulting in decreasing energy spacing for increasing motional quantum number. By adding all contributions from n to $n + m$, the sideband gets smeared out towards the carrier, since the lowest transition $|g, 0\rangle \rightarrow |e, m\rangle$

has the largest frequency. This results in a sideband that has a sharp flank on one side and a smooth tail on the other. The sharp edge can be used to determine the lowest transition's frequency, i.e. the trap frequency obtained by approximating the lattice as a harmonic trap around the minimum.

The harmonic approximation has been made frequently to obtain simple expressions for experimental parameters and to compare the results to the theory available for the harmonic confinement. As motivated in the previous sections and shown by the cartoon in Fig. 4.1, this approximation is not good enough to understand a sideband spectrum from a relatively shallow lattice. As a first order approximation omitting the transversal degrees of freedom and quantum interference between absorption paths, a one-dimensional model of the lattice has been developed. The band structure of the 1D-lattice can be calculated from the theory in Sec. 4.3, which allows placing the individual motional transitions on the spectrum. By assuming the population to be Boltzmann-distributed, a superposition of sub-lines with according peak heights can be fitted to the sideband. Their centers are fixed by the band structure and their width increases due to the broader bands for larger motional quantum number.

The individual transitions inside a sideband will be additionally broadened because of dissipation among the motional states. Fitting the additional broadening allows estimating heating rates due to external noise processes and provides a very accurate tool to observe motional-state dependent effects.

Resolving these vibrational sidebands requires an electronic transition on with a width on the kHz scale to resolve the sidebands at all, but since we are interested in $<$100 Hz scale vibrational effects at frequencies of 10^{15} Hz, one needs an even narrower and extremely stable spectroscopy laser.

The optical lattice provides a highly stable and controllable environment against external noise sources, but cannot completely eliminate them. A study of the various error sources is necessary and will be presented in the remainder of this chapter.

4.5 Parametric heating

A likely source of dissipation processes between motional states in the optical lattice are parametric excitations caused by fluctuations in the lattice intensity or through mechanical noise on optical components. The treatment in this Section follows Savard *et al.* (1997) and Gardiner *et al.* (2000) but drops the harmonic oscillator approximation to use the eigenfunctions derived in Sec. 4.3 to obtain classical rate equations for the parametric heating processes. The classical description is valid for an optical lattice system with sufficient motional decoherence caused by e.g. collisions or coupling to the background blackbody field.

4.5.1 Intensity Noise

Assume a fractional laser intensity fluctuation

$$\epsilon(t) = \frac{I(t) - I_0}{I_0}$$

that modifies the lattice potential according to

$$\tilde{V}(x) = V_0(1+\epsilon(t))\cos^2(\kappa x) \equiv V + V'$$

and produces a small perturbation V' of the original potential. Transition rates between different lattice bands are estimated in first-order perturbation theory as

$$R_{m\leftarrow n} = \frac{1}{T}\left|\int_0^T dt\, e^{i\omega_{mn}t}\langle m|V'|n\rangle\right|^2.$$

Following the arguments in Savard *et al.* (1997), this integral can be approximated as

$$R_{m\leftarrow n} \simeq \frac{1}{\hbar^2}\left|\int_{-\infty}^{\infty} d\tau\, e^{i\omega_{mn}\tau}\langle\epsilon(t)\epsilon(t+\tau)\rangle\right|^2 \times \\ \times \left|\langle m|V_0\cos^2(\kappa x)|n\rangle\right|^2$$

with the noise correlation function

$$\langle\epsilon(t)\epsilon(t+\tau)\rangle = \frac{1}{T}\int_0^T dt\,\epsilon(t)\epsilon(t+\tau) \equiv f(\tau)$$

Assuming $f(\tau) = f(-\tau)$ this expression can be further simplified using the one-sided power spectrum of the fractional noise $\epsilon(t)$

$$S_\epsilon(\omega) := \frac{2}{\pi}\int_0^\infty d\tau\cos(\omega\tau)f(\tau)$$

to obtain a simple expression for the transition rate per particle

$$R_{m\leftarrow n} = \pi S_\epsilon(\omega_{mn})\frac{1}{\hbar^2}\left|\langle m|V_0\cos^2(\kappa x)|n\rangle\right|^2.$$

All sites are equivalent, as the evaluation of the matrix element reduces to an integral on $[0,\pi]$ for all i:

$$\langle i,m|V_0\cos^2(\xi)|j,n\rangle = \delta_{ij}\frac{2}{\pi}\int_0^\pi d\xi\,\mathrm{ce}_m^*(\xi)\cos^2(\xi)\,\mathrm{ce}_n(\xi).$$

The transition rate per particle reads

$$R_{m\leftarrow n} = \pi S_\epsilon(\omega_{mn})\frac{V_0^2}{\hbar^2}\left|\frac{2}{\pi}\int_0^\pi d\xi\,\mathrm{ce}_m^*(\xi)\cos^2(\xi)\,\mathrm{ce}_n(\xi)\right|^2.$$

Remarks

(i) The Mathieu functions ce_n are even (odd) with respect to $\pi/2$ for even (odd) n, although they are all even with respect to 0.
(ii) $\cos^2\xi$ is even with respect to $\pi/2$, so the matrix elements vanish for $|m-n|$ odd.
(iii) Since $\mathrm{ce}_n^* = \mathrm{ce}_n$, $R_{m\leftarrow n} = R_{n\leftarrow m}$.

We will use these transition rates to come up with a set of coupled linear differential equations that determine the behavior of the system. As all particles and sites are equivalent, each rate can be scaled by the number of particles $\mathcal{N}$ to describe the whole ensemble. The rate equations are obtained by writing down all contributions that modify the population of a certain state P_n:

$$\dot{P}_n(t) = -\left(\sum_{m\neq n} R_{m\leftarrow n}\right) P_n(t) + \sum_{m\neq n} R_{n\leftarrow m} P_m(t).$$

Converting this into matrix form results in

$$\dot{\boldsymbol{P}}(t) = S \cdot \boldsymbol{P}(t)$$

with solution

$$\boldsymbol{P}(t) = e^{St} \cdot \boldsymbol{P}_0$$

and system matrix

$$S = \begin{pmatrix} -\sum\limits_{m\neq 0} R_{m0} & 0 & R_{02} & \cdots \\ 0 & -\sum\limits_{m\neq 1} R_{m1} & 0 & \cdots \\ R_{20} & 0 & -\sum\limits_{m\neq 2} R_{m2} & \cdots \\ \vdots & \vdots & \vdots & \ddots \end{pmatrix}.$$

The diagonal elements of the S-matrix correspond to the broadening of the individual sub-lines due to the dissipation modeled here (see Sec. 4.4).

Note that only states which are two motional quanta apart are coupled via this interaction. By experimentally providing initial conditions that put a majority of the population in a certain state, one should be able to observe a large contrast between peak heights of even and odd quantum number n if the dominating noise source is lattice intensity fluctuation.

4.5.2 Phase Noise

A second source of parametric heating could be phase fluctuations of the standing wave pattern, most likely produced by mechanical noise on a fiber tip or mirror mount. This kind of noise can also be described by a fluctuating function $\epsilon(t)$ with $|\epsilon(t)| \ll 1$. Including this noise in the lattice potential amounts to

$$\tilde{V}(x) = V_0 \cos^2(\kappa x + \epsilon(t))$$

Expanding this expression in a Taylor expansion and neglecting terms of second or higher order in ϵ, the potential can again be described as the original lattice potential modified by a small perturbation:

$$\tilde{V}(x) \simeq V_0(\cos^2(\kappa x) + \epsilon(t)\sin(2\kappa x))$$

Using the same formalism as in Sec. 4.5.1, we obtain new transition rates per particle due to lattice phase noise:

$$R^{\mathrm{ph}}_{m\leftarrow n} = \pi S^{\mathrm{ph}}_{\epsilon}(\omega_{mn})\frac{V_0^2}{\hbar^2}\left|\frac{2}{\pi}\int_0^{\pi} d\xi\, \mathrm{ce}_m(\xi)\sin(2\xi)\,\mathrm{ce}_n(\xi)\right|^2$$

The only difference being in the noise spectrum and the matrix element.

Remarks

(i) The matrix elements vanish for $|m-n|$ even, since $\sin 2\xi$ is odd with respect to $\pi/2$.

(ii) Combining the phase noise with the intensity noise transition rates from the previous section, we will obtain a system matrix without zeros, since the new rates fill in the empty spaces.

The system matrix for pure phase noise is

$$S = \begin{pmatrix} -\sum\limits_{m\neq 0} R_{m0} & R_{01} & 0 & \cdots \\ R_{10} & -\sum\limits_{m\neq 1} R_{m1} & R_{12} & \cdots \\ 0 & R_{21} & -\sum\limits_{m\neq 2} R_{m2} & \cdots \\ \vdots & \vdots & \vdots & \ddots \end{pmatrix}$$

Intensity and phase noise show "orthogonal" behavior in coupling levels that are two motional quanta apart, so it should be possible to distinguish between the two by looking at sideband scans after preparing amenable initial conditions and artificially enhancing one or the other process.

4.5.3 Heating Rates

For the harmonic oscillator approximation (see Savard *et al.* (1997)), a heating rate could be defined as the coefficient Γ that appeared when evaluating

$$\langle \dot{E}\rangle = \sum_n \hbar\omega_n \dot{P}_n = \Gamma\langle E\rangle$$

In the optical lattice potential, the equations become more difficult, and a heating rate can only be defined in an average sense depending on the initial conditions. Finding the time T that corresponds to

$$\frac{\langle E\rangle_T}{\langle E\rangle_0} = \exp(1)$$

results in an average heating rate

$$\tilde{\Gamma} := 1/T$$

where the average energy needs to be evaluated by calculating

$$\langle E\rangle_t = \sum_n \hbar\omega_n P_n(t).$$

4.6 Environmental effects

Doing high-precision spectroscopy requires a careful study of potential error sources. This section estimates values for systematics such as the Doppler and Zeeman effects, AC Stark shifts caused by the probing laser or background blackbody radiation as well as altitude shifts. Numerical examples will be calculated for the case of ^{87}Sr atoms at $T = 5\,\mu\text{K}$, lattice (probe) wavelength $\lambda = 813\ (698)\,\text{nm}$ and beam waist $w_0 = 35\,\mu\text{m}$.

4.6.1 Doppler effect

The Doppler effect is the apparent shift in transition frequency caused by an atom moving at a certain velocity with respect to the exciting beam. In the Lamb-Dicke regime, the Doppler effect is suppressed by a factor proportional to the ratio of the particle's mean-free path and the probing wave length (Dicke, 1953). By also probing with a beam that copropagates with the trapping lattice laser, the first order Doppler effect is reduced to the uncertainty limit at the focus of the Gaussian beam, corresponding to

$$\Delta k \times 2w_0 \approx \frac{1}{2}.$$

The uncertainty in the probing wave vector samples some of the transversal motion. We assume the atoms to be *Maxwell-Boltzmann* distributed in three dimensions (i.e. we rely on collisions to thermalize our sample). The probability density function is

$$f^{(3)}(v)dv = 4\pi v \left(\frac{m}{2\pi k_B T}\right)^{3/2} \exp\left(-\frac{mv^2}{2k_B T}\right) dv.$$

Integer moments of this distribution can be computed as:

$$\langle v^n \rangle = \frac{2}{\sqrt{\pi}} \left(\frac{2k_B T}{m}\right)^{n/2} \begin{cases} \sqrt{\pi}\frac{(n+1)!!}{2^{n/2+1}} & n \text{ even} \\ [(n+1)/2]! & n \text{ odd} \end{cases}$$

such that

$$\langle v \rangle = \sqrt{\frac{8k_B T}{\pi m}}$$
$$v_{\text{rms}}^2 := \langle v^2 \rangle = \frac{3k_B T}{m}.$$

This allows putting an uncertainty limit to the observable linewidth caused by the residual first order Doppler effect as

$$\gamma_D^{(1)} = \Delta k\, v_{\text{rms}} = \frac{1}{4w_0}\sqrt{\frac{3k_B T}{m}}$$
$$\frac{\sigma(\gamma_D^{(1)})}{\gamma_D^{(1)}} = \sqrt{\frac{\sigma^2(w_0)}{w_0^2} + \frac{\sigma^2(T)}{4T^2}} \simeq \frac{\sigma(w_0)}{w_0}.$$

In addition to the broadening due to the residual first order Doppler effect, the transition will be shifted by the second order Doppler effect. This is easy to understand if one remembers that the relativistic expression for the Doppler-shifted frequency due to a velocity $\beta := v/c$ is:

$$\frac{\omega}{\omega_0} = \sqrt{\frac{1-\beta}{1+\beta}},$$

which can be expanded for $|\beta| \ll 1$ as

$$\frac{\omega}{\omega_0} = 1 - \beta + \frac{1}{2}\beta^2 + \mathcal{O}(\beta^3).$$

Note that the second order contribution is always positive, regardless of the velocity's sign.

We will again use the root mean square velocity v_{rms} as the characteristic value to estimate the second order Doppler shift and its relative error:

$$\begin{aligned}\Delta\omega_D^{(2)} &= \frac{1}{2}\frac{v_{\mathrm{rms}}^2}{c^2}\omega_0 \\ \frac{\sigma(\Delta\omega_D^{(2)})}{\Delta\omega_D^{(2)}} &= \sqrt{\frac{\sigma^2(T)}{T^2} + \frac{\sigma^2(\omega_0)}{\omega_0^2}} \simeq \frac{\sigma(T)}{T}\end{aligned}$$

For $T = 5(1)\,\mu\mathrm{K}$, $\omega_0 = 2\pi c/\lambda$ and $\lambda = 698\,\mathrm{nm}$, we obtain

$$\begin{aligned}\gamma_D^{(1)} &= 2\pi \times 43(9)\,\mathrm{Hz} \\ \Delta\omega_D^{(2)} &= 2\pi \times 22(5)\,\mu\mathrm{Hz}.\end{aligned}$$

4.6.2 AC Stark shift (probe)

The same effect that forms the lattice will also disturb the states when probing the atoms with another laser. Since we want to scan over a spectral line, we have to introduce a probing laser which will have a very different wavelength than the lattice laser. In our case, the lattice is formed by infrared light at 813 nm, whereas the investigated transition is at 698 nm.

Recall that the maximum AC Stark shift for state $|i\rangle$ is

$$\Delta E_i(\omega) = -\frac{4P}{\pi\epsilon_0 c w_0^2}\alpha_i(\omega).$$

We have to calculate the dynamic polarizabilities of the states involved in our spectroscopic experiment which requires knowledge of the various Einstein A coefficients. The theoretical values for the Einstein A coefficients can be obtained from the extensive list of lifetimes in Werij *et al.* (1992) listed in Tab. 4.1.

Going back to the problem at hand, we are interested in branching ratios of states that can decay to the $^1S_0$ and $^3P_0$ states. The only state coupled to $^1S_0$ via dipole

Electronic state	$\tau^{-1}(10^6\mathrm{s}^{-1})$	$E(10^{15}\mathrm{Hz})$
$5s5p\,^1P_1$	194	4.09
$5s6p\,^1P_1$	2.64	6.427
$5s7p\,^1P_1$	3.05	7.333
$4d5p\,^1P_1$	13.3	7.763
$5s8p\,^1P_1$	14.7	7.761
$5s9p\,^1P_1$	10.9	8.004
$5s10p\,^1P_1$	6.47	8.167
$5s11p\,^1P_1$	4.49	8.282
$5s6s\,^3S_1$	85	2.775
$5s7s\,^3S_1$	34.5	4.356
$5s8s\,^3S_1$	8.22	4.984
$5s9s\,^3S_1$	4.53	5.303
$5s10s\,^3S_1$	2.77	5.487
$5s4d\,^3D_1$	0.345	0.724
$5s5d\,^3D_1$	60.9	3.889
$5s6d\,^3D_1$	27.1	4.781
$5s7d\,^3D_1$	11	5.192
$5s8d\,^3D_1$	7.23	5.419
$5s9d\,^3D_1$	3.27	5.59
$5p^2\,^3P$	119	3.982

Table 4.1: Inverse lifetimes from Werij *et al.* (1992) and energies for ^{88}Sr from Moore (1971). The upper and lower parts of the table list the data necessary to calculate the $^1S_0$ and the $^3P_0$ AC Stark shifts, respectively.

	$\alpha_i(698\,\mathrm{nm})$ (a.u.)	α_i^s (a.u.)
$^1S_0$	340	193
$^3P_0$	965	332
$\Delta\alpha$ (a.u.)	635	139

Table 4.2: Polarizabilities for $^1S_0$ and $^3P_0$ in atomic units: 1 a.u. (polarizability) $= 4\pi\epsilon_0 a_0^3$.

interaction is ${}^1P_1$ which dipole-decays only to ${}^1S_0$, so no branching ratio is needed. The states coupled to ${}^3P_0$ are $5sNs\ {}^3S_1$, $5p^2\ {}^3P_1$ and $5sNd\ {}^3D_1$. We obtain branching ratios of $1/9$, $1/3$ and $5/9$, respectively.

Combining these values with the lifetimes from Tab. 4.1, we get the polarizabilities listed in Tab. 4.2, resulting in an AC Stark shift due to the probing laser

$$\Delta\omega_{\text{probe}}^{\text{AC}} = -2\pi \times 0.6\,\text{Hz} \ @\ 100\,\text{nW}.$$

4.6.3 AC Stark shift (blackbody)

The *blackbody shift* is caused by the thermal background field, resulting in different AC Stark shifts of ${}^1S_0$ and ${}^3P_0$. The magnitude of this effect can be evaluated by equating the integrated blackbody radiation density

$$\rho(T) = \frac{\pi^2 (k_B T)^4}{15\hbar^3 c^3}$$

to the energy density of an electric field $\boldsymbol{E}_0$

$$\rho = \frac{1}{2}\epsilon_0 |\boldsymbol{E}_0|^2$$

lending

$$|\boldsymbol{E}_0|^2 = \frac{2}{15}\frac{\pi^2 (k_B T)^4}{\epsilon_0 \hbar^3 c^3} \simeq 1.38{\times}10^6\,\text{V}^2\text{m}^{-2} \ @\ 300\,\text{K}.$$

The polarizability difference $\Delta\alpha = \alpha({}^3P_0) - \alpha({}^1S_0)$ has been calculated in the previous section to be

$$\Delta\alpha = 139\,\text{a.u. (atomic units)}.$$

The atomic unit of energy is the Hartree energy ε_h, defined in terms of Bohr radius $a_0 = 4\pi\epsilon_0\hbar^2/m_e e^2$ and electron rest mass m_e:

$$1\,\text{Hartree} = \varepsilon_h = \frac{\hbar^2}{m_e a_0^2}$$

We can come up with the atomic unit of electric field strength by dividing the Hartree energy through the electron charge and the Bohr radius

$$1\,\text{a.u. (electric field strength)} = \frac{e}{4\pi\epsilon_0 a_0^2} = 5.142{\times}10^{11}\,\text{V/m}.$$

The transition frequency shift and its relative uncertainty (assuming a temperature uncertainty of 1 K) can be evaluated from

$$\hbar\Delta\omega_{\text{bb}} = -\frac{1}{2}\Delta\alpha |\boldsymbol{E}_0|^2$$
$$\frac{\sigma(\omega_{\text{bb}})}{\omega_{\text{bb}}} = 4\frac{\sigma(T)}{T} \simeq 1\,\%$$

to be

$$\Delta\omega_{\text{bb}} = -2\pi \times 2.39(2)\,\text{Hz}.$$

4.6.4 Second order Zeeman effect

The second order Zeeman effect is caused by the second order perturbation of the linear Zeeman effect and the diamagnetic term of the ^{87}Sr atoms. The Zeeman effect caused by a magnetic field B up to second order is modeled by the Hamiltonian

$$H = H_0 + \frac{\mu_B B}{\hbar}(L_z + 2S_z) + \frac{e^2}{8m_e}B^2 r^2 \sin^2\theta$$

where μ_B is the Bohr magneton and L_z (S_z) is the z-component of the total angular momentum (electron spin) operator. Both contributions to the second order Zeeman effect are small and can be treated in perturbation theory. The diamagnetic term will be treated in first order, whereas the linear term contributes in second order.

Linear term in second order

The linear term

$$H' \equiv \mu_B B(L_z + 2S_z)/\hbar = \mu_B B(J_z + S_z)/\hbar$$

produces a second order energy correction

$$\Delta E_i = -\sum_{f\neq i} \frac{|\langle f|H'|i\rangle|^2}{\hbar\omega_{fi}}.$$

Ignoring hyperfine structure for the moment and working with the fine structure eigenfunctions $|LSJm_J\rangle \equiv |Jm_J\rangle$, the matrix element reduces to $\langle f|S_z|i\rangle$, as the diagonal term is excluded from the sum. By expanding in terms of uncoupled angular momentum functions $|LSm_Lm_S\rangle$

$$|Jm_J\rangle = \sum_{m_L,m_S} |LSm_Lm_S\rangle\langle LSm_Lm_S|Jm_J\rangle,$$

the matrix element can be evaluated as a sum over Clebsch-Gordan coefficients $\langle LSm_Lm_S|Jm_J\rangle$:

$$\langle Jm_J|S_z|J'm_{J'}\rangle = \hbar\delta_{LL'}\delta_{SS'}\sum_{m_L,m_S} m_S\langle Jm_J|LSm_Lm_S\rangle\langle LSm_Lm_S|J'm_{J'}\rangle$$

to obtain

$$\Delta E_i = -\frac{\mu_B^2 B^2}{\hbar}\sum_{f\neq i}\omega_{fi}^{-1}\delta_{L_fL_i}\delta_{S_fS_i}\left|\sum_{m_{L_i},m_{S_i}} m_{S_i}\langle J_f m_{J_f}|L_iS_im_{L_i}m_{S_i}\rangle\langle L_iS_im_{L_i}m_{S_i}|J_im_{J_i}\rangle\right|^2.$$

Note that each term of the first sum contributes with the inverse energy difference between the two states $|f\rangle$ and $|i\rangle$. Contributions will come only from close lying states with the same L and S quantum numbers. For the $^1S_0$ state the shift vanishes, whereas

for $^3P_0$, only the $^3P_1$ state produces a non-zero contribution at $m_J = 0$. The sum evaluates to $-\sqrt{2/3}$ and

$$\begin{aligned}\Delta\omega(^3P_0) &= \frac{2}{3}\left(\frac{\mu_B B}{\hbar}\right)^2 \omega(^3P_1 - {}^3P_0)^{-1} \\ &\simeq 16\,\text{mHz} \;@\; 100\,\text{mGauss}.\end{aligned}$$

Note that this calculation omits hyperfine structure. This can be remedied by applying the hyperfine mixing theory in the last part of this Section.

Diamagnetic term in first order

The diamagnetic term causes a first order energy shift

$$\Delta E_i = \frac{e^2B^2}{8m_e}\langle i|r^2\sin^2\theta|i\rangle.$$

Its magnitude can be estimated easily when knowing that for the low ^{87}Sr states, $\sqrt{\langle r^2\rangle} \approx\ 5 - 10 \times a_0$. We obtain

$$\begin{aligned}\Delta E_i &\approx \frac{e^2B^2}{8m_e}100a_0^2 \\ &\simeq 150\,\mu\text{Hz} \;@\; 100\,\text{mGauss}\end{aligned}$$

Including hyperfine mixing

The hyperfine interaction mixes the singlet and triplet P states, making the clock transition possible. This means that the pure states are not the right candidates to use in the calculation of the Zeeman shift. Instead, we have to find the mixing coefficients and work with superpositions. The treatment in this Section follows Peik *et al.* (1994) where a clock transition in In^+ was examined. The idea is to find the mixing coefficients for the modified $^1P_1$ and $^3P_1$ states caused by hyperfine interaction. Then calculate the superposition corresponding to the $^3P_0$ state in terms of these coefficients in first order perturbation theory. The final states will be $^1S_0$, $^1P_1{}'$, $^3P_0{}'$ and $^3P_1{}'$, where the prime denotes a modified state.

The theory relating hyperfine constants and mixing coefficients was developed by Breit and Wills (1933) and a good mathematical reference is Lurio *et al.* (1962). The hyperfine interaction mixes the $^1P_1$ and $^3P_1$ states as follows:

$$\begin{aligned}|^3P_1{}'\rangle &= \alpha|^3P_1\rangle + \beta|^1P_1\rangle \\ |^1P_1{}'\rangle &= -\beta|^3P_1\rangle + \alpha|^1P_1\rangle\end{aligned}$$

where normalization enforces $\beta = \sqrt{1-\alpha^2}$. These coefficients can be obtained from the lifetimes and transition wavelengths as

$$\frac{\beta^2}{\alpha^2} = \frac{\tau(^1P_1)\lambda^3(^3P_1 - {}^1S_0)}{\tau(^3P_1)\lambda^3(^1P_1 - {}^1S_0)}.$$

The $^3P_0$ state is perturbed through the dipole part of the hyperfine interaction operator $\boldsymbol{K}^{(1)}$ as defined in Lurio *et al.* (1962)

$$\begin{aligned}|^3P_0{}'\rangle &= |^3P_0\rangle + \frac{\langle ^3P_1{}'|\boldsymbol{K}^{(1)}|^3P_0\rangle}{E(^3P_0) - E(^3P_1{}')}|^3P_1{}'\rangle + \frac{\langle ^1P_1{}'|\boldsymbol{K}^{(1)}|^3P_0\rangle}{E(^3P_0) - E(^1P_1{}')}|^1P_1{}'\rangle \\ &\equiv |^3P_0\rangle + \alpha_0|^3P_1{}'\rangle + \beta_0|^1P_1{}'\rangle \\ &= |^3P_0\rangle + (\alpha_0\alpha - \beta_0\beta)|^3P_1\rangle + (\alpha_0\beta + \beta_0\alpha)|^1P_1\rangle.\end{aligned}$$

Expanding the inner products, calculation of the matrix elements reduces to computing $\langle ^3P_1|\boldsymbol{K}^{(1)}|^3P_0\rangle$ and $\langle ^1P_1|\boldsymbol{K}^{(1)}|^3P_0\rangle$ for which algebraic expressions can be obtained from the same paper. They reduce to

$$\langle I^{3,1}P_1Fm|\boldsymbol{K}^{(1)}|I^3P_0Fm\rangle = \sqrt{I(I+1)}\left[\pm\frac{c_{2,1}}{2}(a_s - a_{1/2}) + c_{1,2}\sqrt{2}a'''\right].$$

The constants c_1 and c_2 are related to α and β by

$$\begin{pmatrix}c_1\\c_2\end{pmatrix} = \sqrt{\frac{1}{3}}\begin{pmatrix}1 & \sqrt{2}\\ \sqrt{2} & -1\end{pmatrix}\begin{pmatrix}\alpha\\\beta\end{pmatrix}.$$

The a numbers describe single-electron hyperfine coupling and can be calculated from the hyperfine interval spacings $A(^{2S+1}L_J)$ for $J \neq 0$. The equations are underdetermined and some relativistic correction parameters have to be calculated from theory to obtain numerical values for the a numbers as listed in Heider and Brink (1977). Thus, the final states are known and the differential second order Zeeman shift between $^1S_0$ and $^3P_0$ can be calculated in perturbation theory as demonstated in the previous two Sections. Note that Lurio *et al.* (1962) also list algebraic expressions for all first order Zeeman matrix elements.

4.6.5 Gravitational shift

Absolute frequency measurements are comparisons against some sort of frequency standard. If the frequency standard is located at a different altitude than the experiment, the difference in gravitational field amplitude amounts to a time dilation and thus a global shift in frequency. In the present experiment, absolute frequencies are measured by comparing against an optical-fiber-transferred signal locked to a Cs-standard at NIST Boulder. The Cs clock is located at a larger altitude than the experiment, i.e. under the influence of a gravitational field of lower magnitude. The relative change of the rest wavelength λ_0 in a gravitational field produced by a mass M at distance r is

$$\frac{\lambda}{\lambda_0} = \sqrt{1 - \frac{2GM}{rc^2}}$$

with the gravitational constant G. This translates into a relative change of frequency between our lab frequency ω_l and the Cs clock frequency ω_c (situated at $r_c - h$ and r_c

respectively)

$$\frac{\omega_l}{\omega_c} = \sqrt{\frac{1 - \frac{2GM}{r_c c^2}}{1 - \frac{2GM}{r_c c^2 (1 - h/r_c)}}}$$

which can be expanded in the small parameter $\varepsilon := h/r_c$ as

$$\frac{\omega_l}{\omega_c} = 1 + \left(\frac{r_c c^2}{GM} - 2\right)^{-1} \varepsilon + \mathcal{O}(\varepsilon^2).$$

Using $r_c = 6371.01\,\mathrm{km} + 1640\,\mathrm{m}$, earth's mass $M = 5.9742 \times 10^{24}$ kg and an estimate of the height difference $h = 14(3)\,\mathrm{m}$, we obtain a relative correction

$$\frac{\omega_l - \omega_c}{\omega_c} = 1.5(3) \times 10^{-15}.$$

To get a feeling for its magnitude,

$$\Delta\omega_G \simeq 2\pi \times 0.64(13)\,\mathrm{Hz} \;@\; 698\,\mathrm{nm}.$$

Chapter 5

Precision Spectroscopy in a 1D Optical Lattice

As an application of the theory developed in the previous chapter, precision spectroscopy of the ^{87}Sr $^1S_0 - {}^3P_0$ clock transition in a 1D optical lattice will be presented.

Every spectroscopic experiment can be separated into three conceptual parts: probe, sample and detector corresponding to the $^1S_0 - {}^3P_0$ spectroscopy laser (698 nm), the ^{87}Sr atoms confined in a magic-wavelength 1D optical lattice and fluorescence detection on $^1S_0 - {}^1P_1$ (461 nm) with a *photo-multiplier tube* (PMT). In addition, various trapping and utility lasers help to prepare the sample in a perturbation-free environment.

The spectroscopic data is obtained by scanning the 698 nm laser over the $^1S_0 - {}^3P_0$ resonance. This data must then be referenced to a frequency standard: this experiment uses the NIST F1 Cs standard available via an optical fiber link to a Cs-referenced hydrogen-maser at NIST Boulder. The spectroscopic data is compared to the reference signal by an octave-spanning femtosecond comb. The details of the absolute frequency metrology will be presented in the next chapter.

This chapter will focus on the issues associated with a magic wavelength 1D optical lattice for ^{87}Sr; the sample preparation and pre-cooling steps are described in more detail in several papers from the Ye group (Xu *et al.*, 2002, 2003a,b, Loftus *et al.*, 2004a,b, Ido *et al.*, 2005).

5.1 Atom preparation and MOT cooling

Preparation and initial trapping is described in Loftus *et al.* (2004a) and we shall only summarize the most important steps; see Fig. 5.1 for a detailed picture. Refer to Fig. 5.2 for a detailed energy diagram of ^{87}Sr and the relevant laser wavelengths.

The strong $^1S_0 - {}^1P_1$ transition at 461 nm is used for all of the following preparation of the initial atomic sample. This blue light is produced by frequency-doubling a Ti:Sapphire laser at 922 nm. *Acousto-Optical Modulators* (AOMs) detune the light with

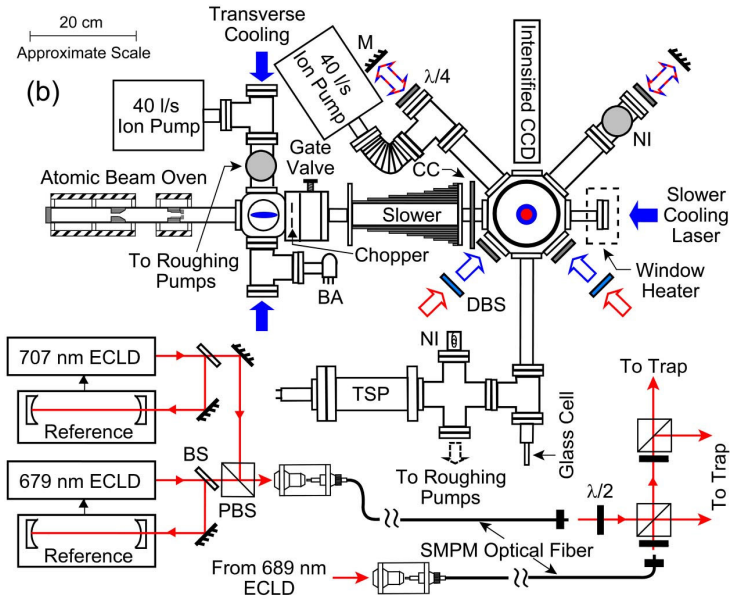

Figure 5.1: Sample preparation and pre-cooling, figure from Loftus *et al.* (2004a)

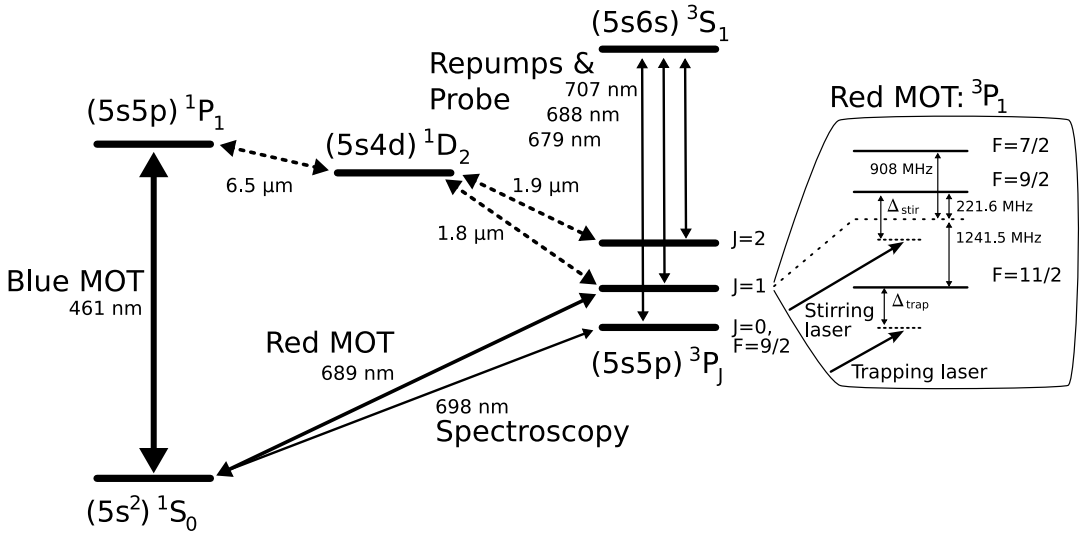

Figure 5.2: Lowest singlet and triplet states of ^{87}Sr

respect to the $^1S_0 - {}^1P_1$ transition in an offset lock using saturated absorption feedback.

The ^{87}Sr atoms are heated in an effusion oven (see upper left of Fig. 5.1) and form a thermal atomic beam that is filtered by an aperture. After passing the aperture, the beam is transversally cooled in a 2D optical molasses. A gate valve and an electrical shutter separate the production region with its hot thermal background from the trap region. The beam is then further cooled in a Zeeman-slower, i.e. a coil producing a magnetic field gradient along the beam direction and a head-on σ^--polarized laser beam. Finally, a standard six-beam MOT captures the atoms at the trap center, where three pairs of Helmholtz coils allow minimizing residual magnetic fields.

Approximately 3×10^7 atoms are captured and cooled by the blue MOT to $T_{\text{blue}} \simeq 2.5\,\text{mK}$. Fluorescence light from the blue MOT is captured on a CCD camera, allowing to monitor the MOT alignment by observing its shape. The metastable $^3P_2$ state ($\tau \sim 500\,\text{s}$) acts as a sink for the MOT population as it removes atoms from the cooling cycle via the spontaneous decay channel $^1P_1 - {}^1D_2 - {}^3P_2$ for a long time (see Fig. 5.2 and Xu *et al.* (2003b)). To counteract the losses into the $^3P_2$ state, population can be pumped to $^3S_1$ from where it subsequently decays to $^3P_1$ (Loftus *et al.*, 2004a).

To further cool the sample, the atoms are then transferred to a narrow-line MOT on the $^1S_0 - {}^3P_1$ transition at 689 nm. This narrow line allows MOT-cooling into the µK regime ($T_D = 180\,\text{nK}$, $T_r = 450\,\text{nK}$). The six beams are introduced into the same beam path as the blue MOT with dichroic mirrors and fluorescence at 689 nm is monitored with a PMT. We manage to transfer roughly 25% of the atoms into the narrow-line MOT, producing a sample at temperatures as low as 250 nK.

As discussed in chapter 3, trapping fermionic isotopes of alkaline earths is very different from the textbook description of an alkali metal MOT. The g-factors of the electronic levels are very different: the upper states $^1P_1$ and $^3P_1$ have much larger g-factors than the ground state $^1S_0$ due to hyperfine interaction (see Sec. 4.6.4). But since the blue transition at 461 nm has a natural linewidth of 32 MHz, the $^1S_0 - {}^1P_1$ MOT still works very well. On the other hand, the red MOT uses the $^1S_0 - {}^3P_1$ transition with a linewidth of 7.1 kHz comparable to the recoil frequency of 4.8 kHz. This makes it necessary to implement the DMOT approach discussed in Sec. 3.2. Two *External Cavity stabilized Diode Lasers* (ECDLs) in a Littman setup were built, one being injection-locked to another diode laser to form a strong trapping beam and one being used as stirring laser (see section 3.2).

The red MOT (689 nm) trapping laser is detuned to the red of the $|^1S_0, F = 9/2\rangle \rightarrow |^3P_1, F = 11/2\rangle$ transition, as shown in the inset on the right hand side of Fig. 5.2, depicting the hyperfine manifold of $^3P_1$. The stirring laser is tuned below the higher lying $|^3P_1, F = 9/2\rangle$ state with its smaller g-factor (Mukaiyama *et al.*, 2003).

5.2 1D optical lattice

After having cooled the atoms into the µK regime, they are slow enough to be loaded into a far-off-resonance trap (FORT) or optical lattice. As shown in chapter 4, it is convenient to use a trapping wavelength that matches the AC Stark shifts of $^1S_0$ and

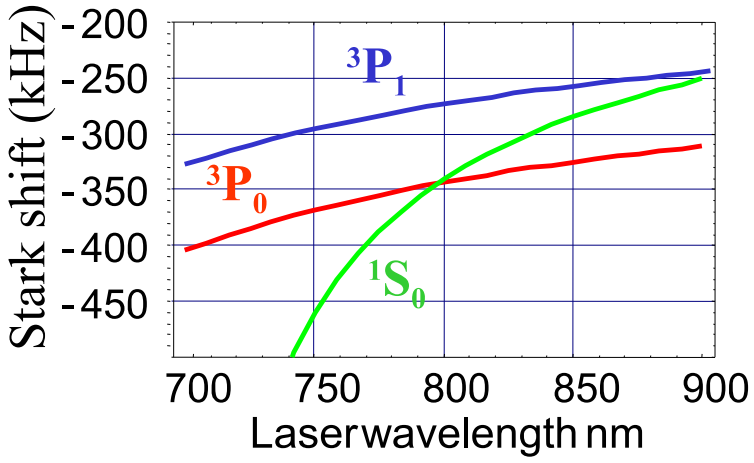

Figure 5.3: AC Stark shifts of the relevant ^{87}Sr levels, figure courtesy of J. Ye

$^3P_0$. In Fig. 5.3, the magic wavelength is shown to lie in the vicinity of 800 nm, with an accuracy limited by the knowledge of the atom's spectrum and oscillator strengths. We experimentally determined the magic wavelength to be 813.418(10) nm by observing the variation of the clock transition linewidth while varying the lattice wavelength.

The figure also shows the AC Stark shift of the $^3P_1$ state. Since it is also shifted negatively, the presence of the strong lattice laser light does not hamper the red MOT cooling process, even in the region where both wavelengths are incident on the atoms. This greatly enhances the lattice loading efficiency since the atoms trapped in the red MOT are forced into the much smaller lattice while still being cooled (transfer efficiency 10 %, lattice lifetime 1 s).

The lattice and spectroscopy lasers are introduced into the trapping chamber via the contraption depicted in Fig. 5.4 and form Gaussian laser beams that are tilted at a small angle with respect to gravity. This vertical mounting ensures that hot sample atoms drop away under the influence of gravity, but also makes it necessary to use a large enough trap depth for the optical lattice. The infrared lattice laser beam leaves fibertip A and gets combined with the spectroscopy beam from fiber B on dichroic mirror D. The copropagation of both beams is of paramount importance to cancel the first order Doppler effect: if the probing beam is not parallel to the trapping beam, it will sample transversal motion and thus broaden the line. The maximal beam divergence is 5 mrad, resulting in an uncertainty of the optical frequency measurement of $\sim$ 1.9 Hz. After entering the trapping chamber through focusing lens L, both beams get reflected back by the highly reflective mirror M. The reflections from this mirror are coupled back into the respective fibers and are used to implement a fiber-noise cancellation protocol. By using the reflection from the mirror situated behind the sample, the fiber-noise cancellation not only reduces noise due to thermal and acoustic vibrations of the fiber, but also of all optical elements up to mirror M. To prevent fiber tip reflections from influencing the noise cancellation, the fiber tips were polished at an angle.

The polarizations of trapping and probing beams need to be matched as well, to avoid

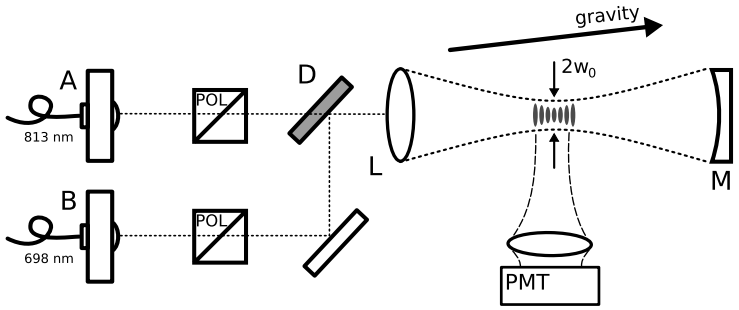

Figure 5.4: Lattice and spectroscopy laser mount (see text).

additional line broadening due to the tensorial nature of the sample's polarizability. The quality of the optical elements, especially the focusing lens, is the main factor introducing mismatch in beam polarizations.

5.3 Spectroscopy

Doing spectroscopy on the ultranarrow ${}^1S_0 - {}^3P_0$ transition makes it necessary to use a laser with a spectral width comparable to the natural linewidth. Building laser oscillators that are stable on the sub-Hz scale requires a highly stable reference cavity. These highly stable cavities are mounted on massive tables which are suspended from the ceiling with rubber bands to minimize sensitivity to accelerations. Acoustic noise is usually attenuated by encasing these mounts with acoustical isolation. All these noise sources perturb the cavity's resonance frequency by varying the cavity's optical length. There is a new scheme on how to get around these large and massive platforms: by mounting the cavity vertically and attaching it to the mount at specific points, the differential change in optical length below and above the mounting point can be compensated to first order.

The spectroscopy laser is an ECDL locked to the reference cavity in a Pound-Drever-Hall locking scheme. In a beat experiment against another sub-Hz laser system, the spectroscopy laser has shown a linewidth <3 Hz (Notcutt *et al.*, 2005). Since the cavity spacer is made out of Zerodur, it has very good short-term stability, but shows a residual mechanical drift rate on the order of 7 Hz/s. This would make the laser unusable for spectroscopy of such a narrow line, so the drift has to be compensated for. A drift compensation scheme that also allows scanning the laser frequency over the ${}^1S_0 - {}^3P_0$ resonance will be presented in detail in chapter 6. For the remainder of this chapter, we will assume that we have a perfectly stable and tunable probe that is referenced to a frequency standard and focus on the issues arising from the confinement geometry and the specifics of ^{87}Sr.

The spectroscopy signal is obtained by observing the fluorescence on the strong ${}^1S_0 - {}^1P_1$ transition as a measure of the ${}^1S_0$ population. Doing a Rabi flop on the narrow ${}^1S_0 - {}^3P_0$ transition is inefficient since the Rabi frequency varies over the radial extent of the probing beam. Thus, the metastable ${}^3P_2$ state is used to store population in the

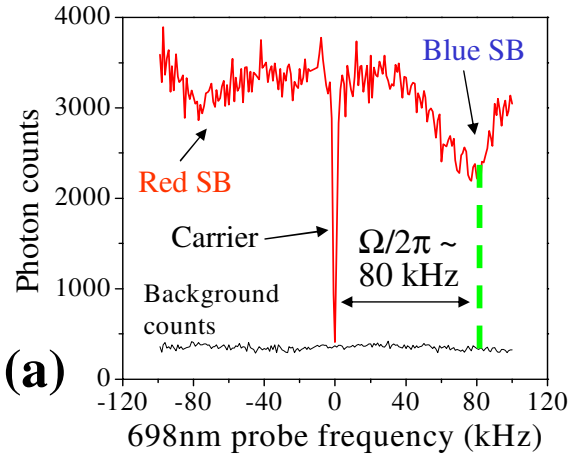

Figure 5.5: Typical spectrum of the $^1S_0 - {}^3P_0$ resonance with vibrational sidebands, figure from Ludlow *et al.* (2005).

following way: A π-pulse at the maximal Rabi frequency is shone onto the sample. Then, population is excited to $^3P_2$ by driving the $^3P_0 - {}^3S_1$ transition which decays to $^3P_1$ and $^3P_2$ ($\gamma = 2\pi \times 1.4\,\mathrm{MHz}$). By repeating this probing and shelving cycle 20 times for each point in the spectral scan, the fluorescence signal can be nulled almost completely in the resonant case. This works because the atoms in the $^1S_0$ state have a finite temperature and rethermalize on a much shorter timescale than the $^3P_2$ lifetime (500 s).

When first starting to measure narrow spectra of the transition in question, we found vibrational sidebands as discussed in section 4.4. These sidebands are very convenient for quickly checking important system parameters. The distance of both the red and the blue sideband's outer flank from the carrier is the transition frequency from the motional ground state to the first excited state. Since the harmonic approximation fits best for the lowest-lying motional states, fitting a half-Lorentzian to the outer flank and fitting a Lorentzian to the carrier returns the longitudinal trap frequency ω_z. Next, the relative height of the blue and red sideband returns the temperature in the harmonic approximation, assuming a Boltzmann distribution. Finally, the ratio of carrier and sideband peak heights is related to the Lamb-Dicke parameter η (Wineland and Itano, 1979).

Doing this preliminary analysis on the data shown in Fig. 5.5 gives $\omega_z = 2\pi \times 80\,\mathrm{kHz}$, $T = 5\,\mu\mathrm{K}$ and $\eta = 0.23$.

Applying the theory developed in chapter 4, we can do a bit better, though: By fitting a superposition of Lorentzians to the sideband we can get the lattice parameters more accurately, due to being able to calculate the motional spectrum beforehand. As was discussed in section 4.4, we can use the trap frequency determined by the sharp flanks of the sidebands to calculate the q-parameter which completely determines the spectrum. This has been done for $\omega_z = 2\pi \times 80\,\mathrm{kHz}$ in Tbl. 5.1. Thus we can fixate the individual sub-lineshapes relative to the sharp flank and fit a superposition of Lorentzians – with decreasing peak heights corresponding to a Boltzmann distribution – to the sideband.

n	$E(E_{\mathrm{rec}})$	$\Gamma(E_{\mathrm{rec}})$	E(kHz)	Γ(Hz)
0	11.23	10^{-8}	38.97	10^{-4}
1	33.16	10^{-6}	115.06	0.009
2	53.97	10^{-4}	187.24	0.360
3	73.53	0.002	255.13	8.384
4	91.68	0.036	318.09	124.406
5	108.01	0.359	374.76	1243.010
6	121.42	2.185	421.28	7580.502

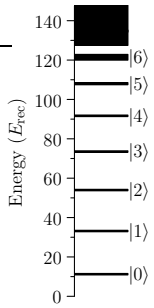

Table 5.1: Band structure of the 1D optical lattice for a trap frequency of 80 kHz

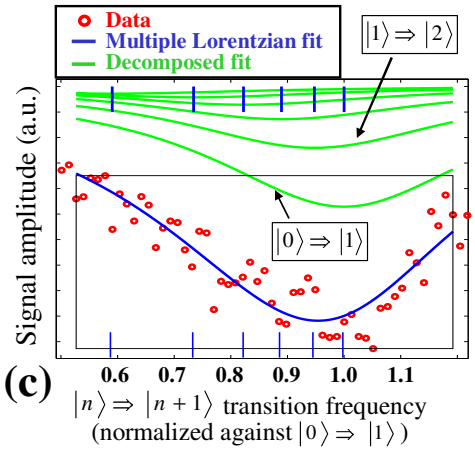

Figure 5.6: Multiple-Lorentzian fit to the blue sideband in Fig. 5.5, figure from Ludlow *et al.* (2005)

The fit lends a more accurate measure of the longitudinal temperature; an example for the blue sideband is shown in Fig. 5.6. The bumpy structures especially apparent in the red sideband of Fig. 5.5 are very well matched with the centers of the sub-lineshapes.

The temperature obtained from the Boltzmann distribution of the peak heights also matches the 5 µK obtained by taking expansion pictures. The trap depth calculated from the observed trap frequency is ∼20 µK matching the design parameters very well. We see significant (∼ kHz) broadening of the sub-lineshapes in addition to the broadening given by the band structure, indicating strong motional dissipation. These dissipative processes make our model of incoherently adding Lorentzians even more valid, as the system's coherences decay rapidly.

In conclusion: motional sideband spectroscopy is an accurate tool to obtain trap characteristica. It is doubly beneficial because it allows monitoring of experimental parameters without modifying the setup. By doing high-resolution scans of the motional sidebands it will be possible to quantify state-specific effects, such as dissipation processes broadening each motional state (see Sec. 4.5).

Finding the sideband structures was serendipical and not the main goal of the experi-

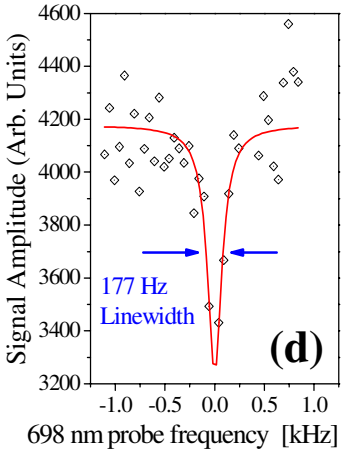

Figure 5.7: Typical spectrum of the ${}^1S_0 - {}^3P_0$ transition, figure from Ludlow *et al.* (2005)

ment. We proceeded to zoom in on the carrier and tried to minimize its width. A typical scan with a linewidth of less than 200 Hz is shown in Fig. 5.7. The measured linewidth is much larger than the theoretically predicted 8 mHz and the uncertainty limit of ~ 50 Hz, due to several systematic effects.

Many of the broadening and shifting effects have already been discussed in Sec. 4.6, but some have to be determined experimentally, because the theory lacks accurate knowledge of important atomic parameters such as the scattering length.

An example for such an experimentally determined systematic is the density shift: at µK-temperatures, scattering becomes a purely quantum-mechanical process. The interatomic molecular potentials vary depending on the average particle spacing, causing transition frequencies to shift. This is usually a very small effect ($\sim$ mHz) and only noticable due to the extremely high precision necessary for an optical clock experiment (Gibble and Chu, 1993, Legere and Gibble, 1998). As shown in Fig. 5.8, we varied the atomic density inside the lattice by a factor of 50 and fitted a linear function to the center frequency data to obtain an upper limit on the density shift: $1.0(6.4)\,\mathrm{Hz}/(10^{12}\mathrm{cm}^{-3})$.

The second experimentally determined systematic is the Zeeman shift due to residual magnetic fields or an anisotropic population distribution among the lower state's magnetic substates. By using the three pairs of compensation coils, we determined a first order Zeeman shift of -32(7) Hz/Gauss (see Fig. 5.9). The magnetic field uncertainty is less than 400 mGauss, corresponding to an uncertainty of 12 Hz in the frequency measurement.

Finally, the AC Stark shifts due to the incident lattice and probe lasers were determined experimentally. By inserting an EOM into the probe laser path, we were able to vary the probing intensity while retaining a strong off-resonant carrier frequency to use for the fiber-noise compensation discussed in the last section. We obtained -17(8.3) and 7.0(0.9) Hz for the lattice and probe AC Stark shifts, as shown in Fig. 5.10 for the shift caused by the lattice laser.

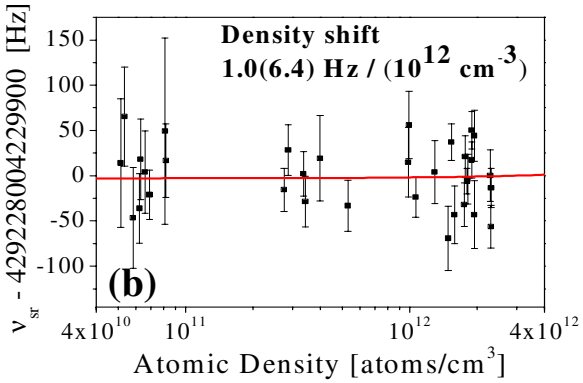

Figure 5.8: Density shift, figure from Ludlow *et al.* (2005)

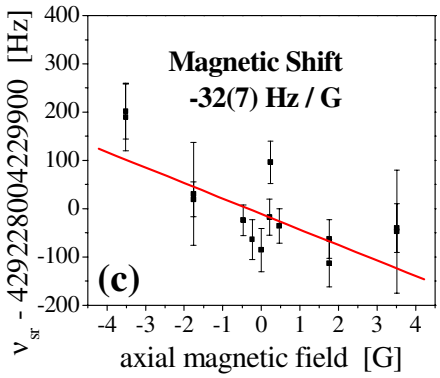

Figure 5.9: Magnetic shift, figure from Ludlow *et al.* (2005)

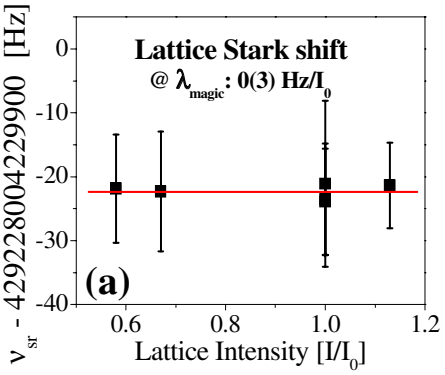

Figure 5.10: Lattice AC Stark shift, figure from Ludlow *et al.* (2005)

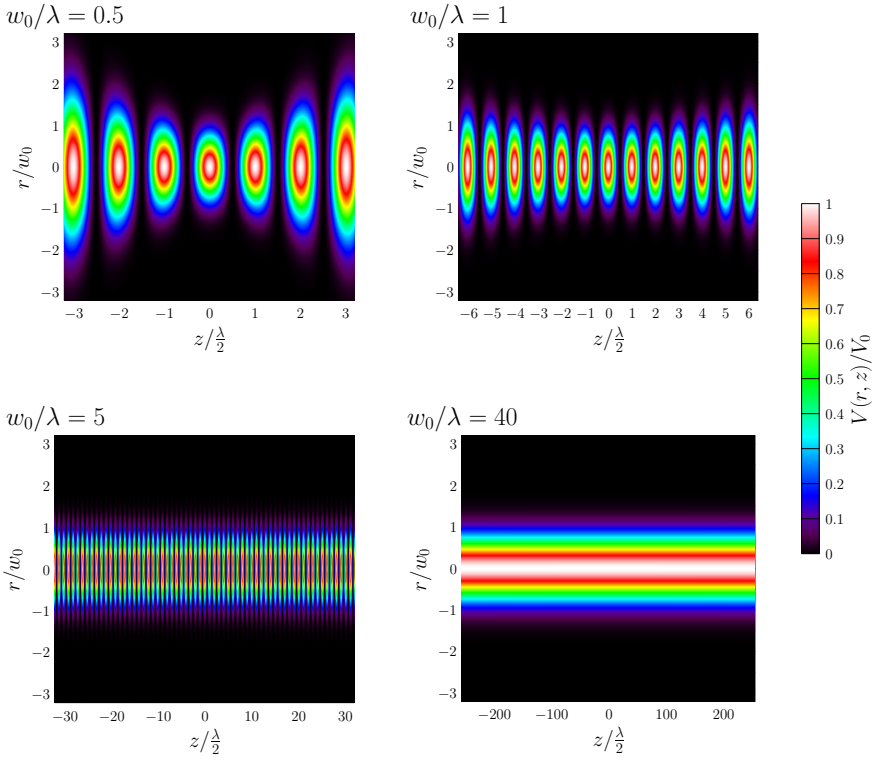

Figure 5.11: Lattice curvature for ratios $w_0/\lambda = \{0.5, 1, 5, 40\}$

Another concern is that the geometry of the 1D optical lattice might adversely affect the width of our spectra. To answer this question, we will try to get a better feeling for the lattice shape by deriving some additional system parameters. Expanding the lattice potential Eq. 4.1 to second order around a minimum lends the ratio between trapping frequencies

$$\frac{\omega_r}{\omega_z} = \frac{\lambda}{\sqrt{2}\pi w_0} \simeq 5 \times 10^{-3}, \tag{5.1}$$

obtaining a transversal trap frequency $\omega_r = 2\pi \times 0.4\,\mathrm{kHz}$ at a lattice waist $w_0 = 35\,\mu\mathrm{m}$. The lattice has ∼400 sites with typically 250 atoms per site, i.e. spatial densities of $2 \times 10^{12}\,\mathrm{cm}^{-3}$. Each populated lattice site looks the same. This is true because the ratio of $w_0/\lambda \simeq 43$ produces a cylindrically symmetric standing wave in the longitudinal dimension for the populated region around the focal point of the lattice beam. This amounts to approximating $w(z) \simeq w_0$ in Eq. 4.1. In Fig. 5.11, the lattice potential is plotted for different ratios w_0/λ. Note that the z-axis is scaled differently for each subplot and that only the curvature of the envelope changes.

Still, a one-dimensional optical lattice is not really a one-dimensional system. This becomes very apparent when comparing the relevant energy scales to the transversal level spacing: due to the non-separability of the Gaussian beam potential into longitudinal and transversal degrees of freedom, the transversal trapping frequency will always be several

orders of magnitude less than its longitudinal counterpart. Being in the longitudinal ground state cannot guarantee being in the transversal ground state. Even worse, by focusing the lattice beam more tightly, this inequality deteriorates even more as shown by Eq. 5.1. This means that atoms in the longitudinal ground state are highly excited in the transversal degrees of freedom. In the sense of the experiments on Tonks-Girardeau gases[1], this is not a one dimensional system. But since the transversal level splitting is so small, we can treat the particle as being quasi-free in the transversal direction, i.e. small changes in the particle's transversal energy do not affect its longitudinal state.

The separation into two different harmonic oscillators is also not correct: the potential is not separable after all, even though all sites might look the same. This means that the longitudinal trap frequency changes when moving away from the lattice axis. These geometric effects make an accurate determination of the motional sideband spectrum difficult, but do not affect the carrier line width to first order for the following reasons:

- The transversal motion is not sampled to first order, i.e. the first order Doppler effect is cancelled by using a copropagating probe beam.
- The sample temperature is $\sim 5\,\mu\mathrm{K}$, resulting in an average longitudinal quantum number $\langle n_z \rangle \simeq 1$. Therefore, a large percentage of the population is in the longitudinal ground state, which shows much less dissipative broadening than the excited motional states.

Over the course of several months, we were consistently able to produce spectra of the ${}^1S_0 - {}^3P_0$ transition which were referenced to the NIST F1 Cs-fountain clock using the scheme described in the next chapter. The low instability of the reference allowed relatively rapid averaging of the transition frequency. A summary of our results and an outlook towards improvements and future experiments will be presented in chapter 7.

[1] A quasi one-dimensional quantum gas of bosons, produced by transferring a BEC into a 3D optical lattice with high aspect ratio. These systems achieve $\omega_r/\omega_z \simeq 10$ such that $\hbar\omega_r$ is the largest energy scale in the system, making it highly unlikely to be radially excited by any longitudinal process (Paredes *et al.*, 2004).

Chapter 6

Determining Absolute Frequency

What do we mean by measuring frequency? Recall the discussion in Sec. 1.1: every frequency measurement is a comparison of one oscillator against another oscillator which is defined as the frequency standard. The frequency standard used in determining the optical frequencies in the ^{87}Sr spectroscopy experiment as discussed in the previous chapter is a Cs-fountain clock at NIST Boulder. Since the standard is not situated in the same lab, its signal needs to be transferred from NIST, which is several km away. Frequency transfer via a frequency-modulated hydrogen maser transmitted over an optical fiber link has proven to be sufficiently stable (Ye *et al.*, 2003).

Once the maser signal arrives at the lab, its modulation frequency at 950 MHz is detected. With the help of a femtosecond comb, this radio frequency is compared against the spectroscopy laser at 698 nm. The beat between the maser signal and the down-scaled optical frequency is counted on a frequency counter (~ 10 kHz). This beat note can be scaled up again to the optical regime, thereby putting a frequency scale on the spectroscopic data.

This chapter will introduce the elements of the setup, but will concentrate on the electronics and software used for counting the optical frequency. Additionally, a feedback scheme for dynamical compensation of residual cavity frequency drift (~ 7 Hz/s) will be presented. The other elements such as the femtosecond comb, the spectroscopy laser and the reference cavity are explained in much greater detail elsewhere (see references throughout the chapter).

In Fig. 6.1, the setup for doing the frequency comparison is depicted schematically. The next section will be devoted to going through the whole figure and explaining in detail the different parts involved in counting optical frequencies.

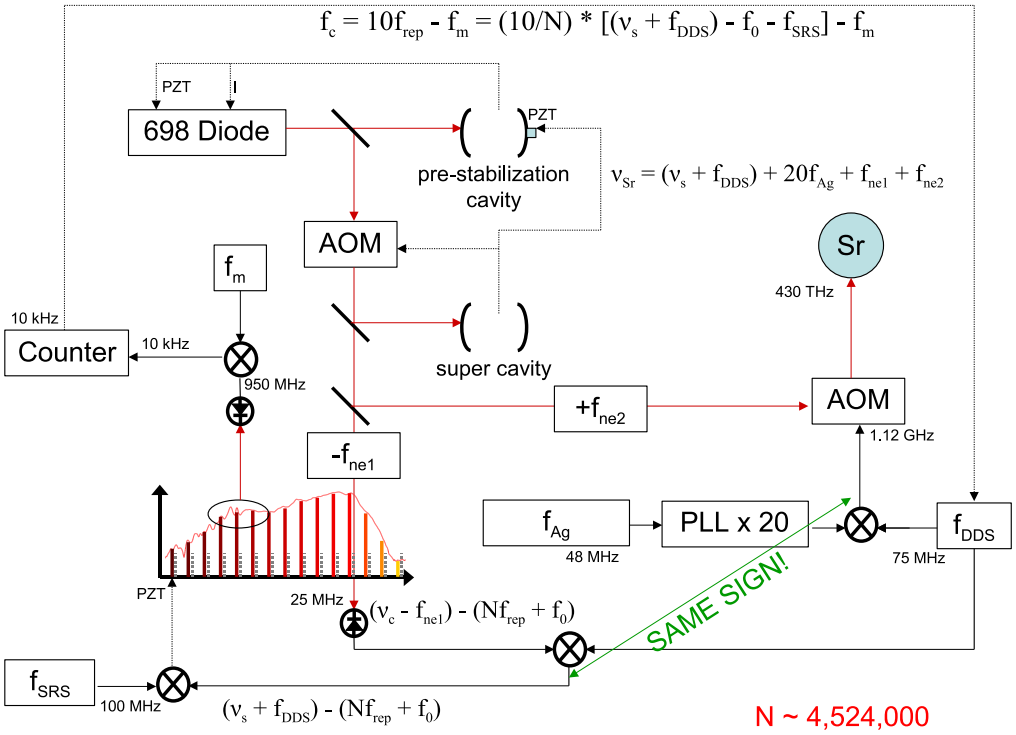

Figure 6.1: Schematic of the frequency metrology setup, figure courtesy of S. Foreman

6.1 Schematic

We shall begin in the upper left corner of Fig. 6.1: the spectroscopy laser system consists of a laser diode in a Littman setup emitting light at 698 nm. Two feedback loops control the wavelength by modifying diode current and backcoupling mirror position (by changing the voltage on a Piezo crystal). After roughly matching the laser's wavelength to a pre-stabilizing cavity by observing the transmitted light on a CCD camera, these feedback loops stabilize the diode wavelength using the Pound-Drever-Hall locking technique (see Hall *et al.*, 2001, for more details on such a setup).

The pre-stabilized laser beam passes an AOM, a small part gets split off and is introduced to the reference cavity. Again, by monitoring the cavity transmission and steering the pre-stabilization cavity length with a Piezo crystal, the first cavity and thus the diode laser wavelength is matched to the transmission frequency of the reference cavity. Two feedback loops on the AOM and the pre-stabilization cavity length lock the laser frequency to the reference at ν_c.

The reference cavity is made out of a Zerodur spacer and uses a novel vertical mounting scheme that minimizes cavity length sensitivity to vertical accelerations such as gravity.

This scheme is so effective that the cavity can be placed on a simple spring-compensation platform and makes large-scale large-mass setups unneccessary (Notcutt *et al.*, 2005). Due to using a Zerodur spacer, the cavity has a residual mechanical frequency drift of 7 Hz/s that makes it very difficult to use the laser to do spectroscopy on the 10 Hz level. To counter this frequency drift, a digital feedback loop measures the drift and compensates for it by controlling the AOM placed before the ^{87}Sr sample on the right hand side of the figure.

First, the optical frequency has to be measured, though: the spectroscopy laser signal is split and coupled into two optical fibers which transport the signal to two different optical tables. Each of these fiber links introduces noise on the signal mostly due to acoustic noise and thermal effects. This noise is compensated for by a fiber noise cancellation protocol using an AOM to dynamically counter any noise detected on the reflection from the tip on the far end of the fiber. The AOM used to transmit to the fs-comb (atomic sample) shifts the signal by $-f_{\mathrm{ne1}}$ ($+f_{\mathrm{ne2}}$). These frequencies are derived from an RF oscillator running at $f_{\mathrm{rf}} = 155.46464\,\mathrm{MHz}$ and obey $f_{\mathrm{rf}} = f_{\mathrm{ne1}} + f_{\mathrm{ne2}}$.

On the comb table[1], the signal at $\nu_s := \nu_c - f_{\mathrm{ne1}}$ is heterodyned against a tooth of the comb at $\nu_N := N f_{\mathrm{rep}} + f_0$, producing a beat note $\nu_s - \nu_N \approx 25\,\mathrm{MHz}$ which is detected on a photo detector. The beat note is electronically mixed with the signal $f_{\mathrm{DDS}} \approx 75\,\mathrm{MHz}$ from the cavity drift compensating oscillator. The mixed signal is again mixed down with $f_{\mathrm{SRS}} = 100\,\mathrm{MHz}$ from another RF oscillator. The final signal then controls a Piezo crystal in the femtosecond comb with a feedback loop, locking the comb's repetition rate f_{rep}, such that

$$(\nu_s + f_{\mathrm{DDS}}) - (N f_{\mathrm{rep}} + f_0) = f_{\mathrm{SRS}}. \tag{6.1}$$

The comb's other free parameter f_0 is also locked with a feedback loop to 70 MHz. By fixing both of the comb's free parameters, it works as a translation gear between an optical frequency ν_c and a microwave frequency f_{rep}.

The repetition rate of a femtosecond comb can easily be detected if its spectrum spans a whole octave: by frequency-doubling a low-lying comb tooth and beating it against a high-lying one, one obtains a beat note at f_{rep} and its harmonics. In the present case, the tenth harmonic of the repetition rate is detected with a photo detector. This signal is then beat against the maser frequency at 950 MHz, resulting in a signal at $f_c \approx 10\,\mathrm{kHz}$ which is then counted with an electronic frequency counter. It can be converted back into an optical frequency by inserting Eq. 6.1:

$$f_c = 10 f_{\mathrm{rep}} - f_m = \frac{10}{N}\left[(\nu_s + f_{\mathrm{DDS}}) - f_0 - f_{\mathrm{SRS}}\right] - f_m. \tag{6.2}$$

The frequency counter is controlled with a Labview program that takes a chunk of frequency data every 30 s and fits a linear function to it to determine a frequency drift rate due to the drifting reference cavity. The program then programs a programmable oscillator (with output frequency f_{DDS}, see right hand side of the figure) to emit a corresponding linear frequency ramp starting at roughly 75 MHz. This frequency ramp

[1] A description of the octave-spanning femtosecond comb system can be found in Fortier *et al.* (2003).

is then mixed with a signal from a VCO which is phase-locked to another programmable oscillator (f_{Ag}) with a frequency multiplication factor of 20.

The mixed signal (1.12 GHz) controls the previously mentioned drift compensating AOM, such that the final frequency ν_{Sr} introduced to the atomic sample is

$$\nu_{\mathrm{Sr}} = (\nu_s + f_{\mathrm{DDS}}) + 20 f_{\mathrm{Ag}} + f_{\mathrm{ne1}} + f_{\mathrm{ne2}}. \tag{6.3}$$

6.2 Features and Remarks

Since so many oscillators, counters and lasers are involved in comparing the NIST standard against the ^{87}Sr transition frequency, one has to worry about the accuracy of very many parts. Thus it is very important that *every* oscillator and electronic counter is referenced to the same highly stable electronic reference. We use a commercial Cs clock situated in the lab, whose 10 MHz signal is split to all the electronic parts with a distributing amplifier.

The most critical electronic part is the frequency counter counting the beat between the maser signal and the comb repetition rate. It is an HP53132a counter by Agilent[2]. These counters take data at a their reference clock frequency of 10 MHz and thus obtain a whole array of frequency data during the gate time of 1 s. A sine function is then internally fitted to that data allowing a measure of the counted frequency on the µHz level within 1 s. The counter's accuracy has been tested by independently counting the same signal with two of the counters and comparing their result.

The counter must be so accurate because the data it produces will be converted into an optical frequency by inverting Eq. 6.2 and inserting into Eq. 6.3 to obtain

$$\nu_{\mathrm{Sr}} = \frac{N}{10}(f_c + f_m) + f_0 + f_{\mathrm{SRS}} + 20 f_{\mathrm{Ag}} + f_{\mathrm{rf}}, \tag{6.4}$$

thus multiplying the counted frequency with the huge comb index $N \approx 4524000$. If the counter is off by 1 Hz, the resulting optical frequency will be off by half a MHz. The same level of accuracy is also required of the maser frequency f_m for the same reason.

In contrast to that, it does not matter too much if the other RF frequencies involved in determining ν_{Sr} are off by 1 Hz, since their inaccuracy directly translates into the optical regime. Also note that f_{rep} and f_{DDS} do not show up at all in Eq. 6.4, i.e. they are in-loop variables and do not need to be accurately known at all.

Also note that the comb index N might change each time the whole system is re-locked. Actually, N is determined by guessing $\nu_{\mathrm{s}} + f_{\mathrm{DDS}} = \nu'$ from its value on the previous day of measurement and a typical cavity drift of 7-8 Hz/s. To find the spectroscopy transition again, the system is locked up and some preliminary data at f_c is counted. By using Eq. 6.2, a value N' is estimated as

$$N' = \frac{10}{f_c + f_m}(\nu' - f_0 - f_{\mathrm{SRS}})$$

[2] See `http://www.agilent.com`.

which never differed by more than 10^{-3} from an integer. So N is calculated by rounding N' and a corresponding value of f_{Ag} is calculated from prior knowledge of ν_{Sr} by using Eq. 6.4. Then the programmable oscillator producing f_{Ag} is tuned until a spectroscopy signal is found. This is convenient because f_{Ag} is also used to step the spectroscopy laser over the transition to obtain a spectrum.

The remainder of this chapter will focus on the implementation of the drift-compensation electronics and software, i.e. the programmable oscillator producing f_{DDS}, the programmable frequency multiplier scaling f_{Ag} and the software controlling them.

6.3 Frequency Multiplier

As another technical application of the phase-locked loop theory developed in Sec. 1.2, a USB programmable frequency multiplier with a target range of 500 MHz to 1 GHz is presented. The small box can be plugged into any personal computer running the Windows operating system and provides convenient access to the GHz regime.

The box uses the ADF4111 PLL chip by Analog Devices[3]. Although it was originally designed for cell phone applications and thus is a tiny surface-mount device, it has several interesting features that make its use worthwhile:

- digital phase-frequency detector as discussed in Sec. 1.2.3
- error signal provided by a charge-pump with programmable amplitude
- two dividers with large programmable division ratios on the reference and VCO inputs
- accepts 3.3 V or 5 V power supply voltage

A schematic of the box can be found in Fig. 6.2. The ADF4111 chip is programmed via a USB digital I/O card from DeVaSys[4]. The error signal provided by the ADF4111 chip is filtered and amplified with a custom loop filter to match the requirements of the Minicircuits MCL-POS1000W VCO. The VCO output is split into two parts: one is the output signal and one is fed back into the ADF4111 to be divided down and compared against a fraction of the reference clock. The division ratios as well as several locking schemes can be programmed via the USB board.

6.3.1 Circuit

The experiment required a programmable frequency source around 0.9-1.0 GHz, so the parts were chosen accordingly. The ADF4111 is specified for output frequencies between 80 MHz and 1.2 GHz, the Minicircuits MCL-POS1000W is a wide band linearly tunable VCO working between 0.5 and 1.0 GHz. The splitter is a Minicircuits MCL ZFSC-2-4 for frequencies between 0.2 and 1000 MHz.

The circuit diagram for the ADF4111 board is shown in Fig. 6.3. The RF inputs J_1 (reference) and J_2 (VCO) are AC-coupled and can be set to 50 Ω input impedance by adding 51 Ω SMD resistors at R_1 and R_2. There is an additional RF input RFINB (pin 5)

[3] Analog Devices ADF4111, see `http://www.analog.com`

[4] DeVaSys USB I2C/IO card, see `http://www.devasys.com/usbi2cio.htm`

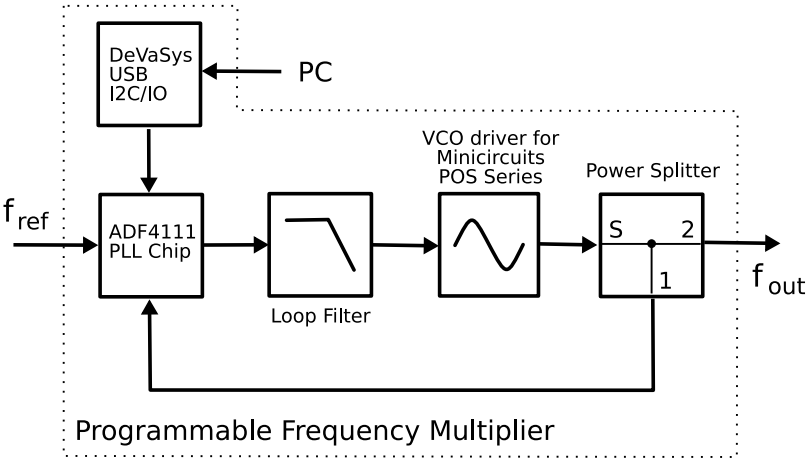

Figure 6.2: Frequency multiplier schematic

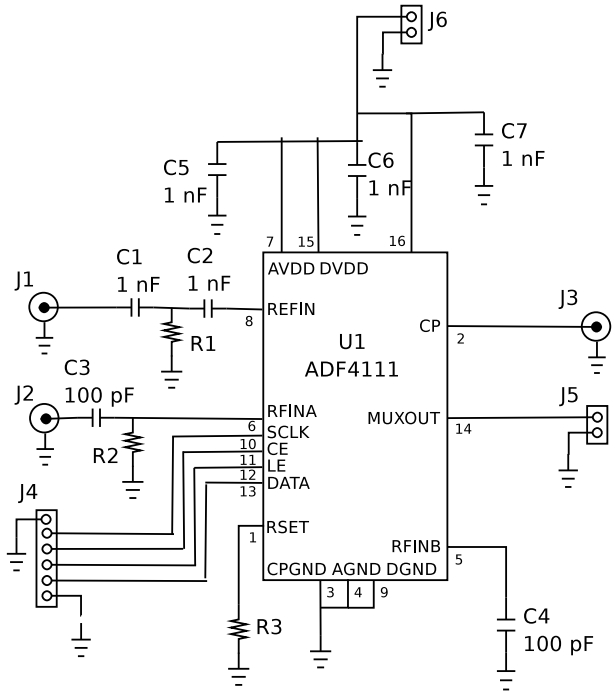

Figure 6.3: ADF4111 circuit

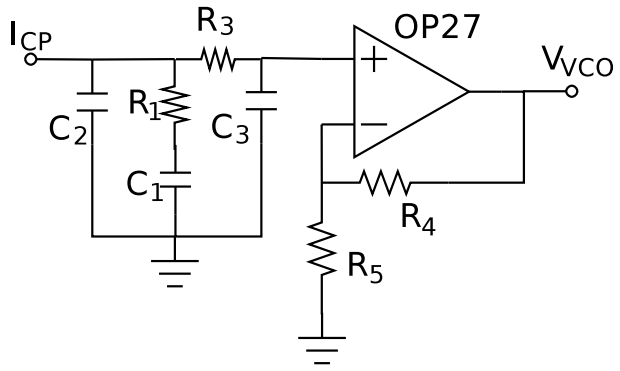

Figure 6.4: Loop filter circuit

which gets subtracted from the VCO input RFINA (pin 6); it is unused and AC-coupled to the ground plane. The supply voltage for the PLL chip on J_6 was chosen to be 3.3 V as the USB I/O card programming the chip uses 3.3 V CMOS logic. All power supply pins use 1 nF decoupling capacitors. The chip is programmed via the four lines of J_4 and offers a programmable monitor at J_5. As an indicator that the signal is locked, J_5 is connected to an LED. The error signal is provided at J_3 and its output range is set by choosing R_3 — 4.7 kΩ are used corresponding to a maximum current from 0.63 mA to 5.00 mA as set by the software. No loop filter is included on this board, but as the VCO accepts positive voltages up to 16 V it becomes necessary to amplify the error signal.

The schematic for the loop filter is given in Fig. 6.4. The ADF4111 error signal output at J_3 is a charge-pump, i.e. a *current source*. This current has to be converted into a control voltage using the parallel combination of capacitances C_1 and C_2. By adding an additional resistor R_1, the resulting voltage is already low-pass filtered. This can be seen easily, as the impedance of the conversion stage is[5]

$$Z_{12} = \frac{1}{sC_2} \parallel (R_1 + \frac{1}{sC_1}) = \frac{s\tau_1 + 1}{s(C_1 + C_2)(s\tau_{12} + 1)}$$

with time constants $\tau_1 := R_1 C_1$ and $\tau_{12} := R_1(C_1 \parallel C_2)$. The voltage after the input stage is $v = Z_{12} i_{\mathrm{cp}}$ with i_{cp} being the current from the charge-pump to ground through the input stage. The input signal is the charge-pump current which is proportional to the phase error detected by the PLL chip. The output signal is the voltage v after the stage, so the impedance Z_{12} is the transfer function determining the frequency response of this sub-circuit.

The second part of the loop-filter is low-pass filtering v with a time-constant $\tau_3 := R_3 C_3$ resulting in a control voltage which is amplified with a non-inverting amplifier configuration of gain $g = 1 + R_4/R_5$. The total transfer function is read off from

$$v_{\mathrm{ctrl}} = g\frac{1}{1 + s\tau_3} v = g\frac{s\tau_1 + 1}{s(C_1 + C_2)(s\tau_{12} + 1)(s\tau_3 + 1)} i_{\mathrm{cp}}.$$

[5]The operation $\parallel$ is defined as $x \parallel y := xy/(x + y)$.

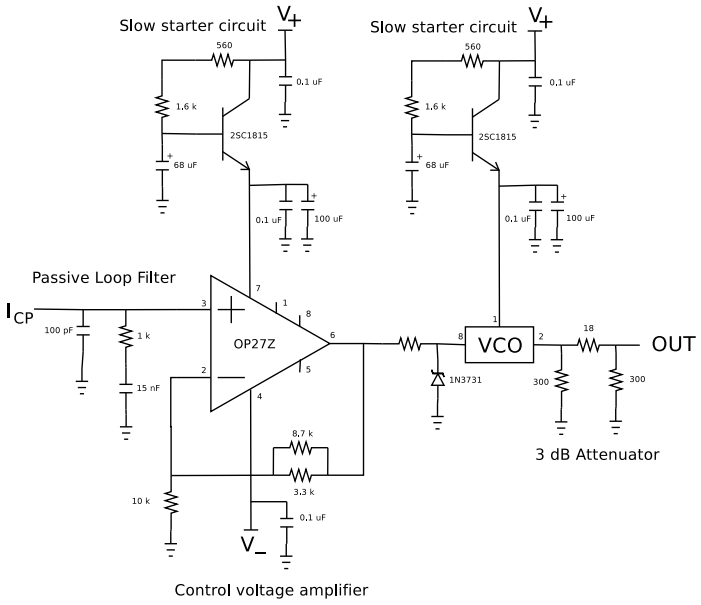

Figure 6.5: Final Loop filter and VCO driver circuit

The effect of the loop filter is: an input current is converted into a voltage which is low-pass filtered two times and then amplified with a constant gain factor.

An amplification factor of ~ 5 proved sufficient to cover the desired frequency range, so the circuit uses $R_4 = 10\,\mathrm{k\Omega}$ and $R_5 = 3.3\,\mathrm{k\Omega} \parallel 8.7\,\mathrm{k\Omega} = 2.4\,\mathrm{k\Omega}$. The combination producing the least amount of ringing and fastest locking time was found to be $C_2 = 100\,\mathrm{pF}$, $C_1 = 15\,\mathrm{nF}$, $R_1 = 1\,\mathrm{k\Omega}$, resulting in a corner frequency $f_{12} = (2\pi\tau_{12})^{-1} = 1.6\,\mathrm{MHz}$. The low-pass filter (R_3, C_3) was finally omitted, since the loop characteristics did not seem to improve.

An existing VCO driver board for the MCL-POS series was modified to accommodate the loop filter and the power supply connections. The final circuit is depicted in Fig. 6.5. The $\pm 15\,\mathrm{V}$ power supply is decoupled from VCO and operation amplifier with slow-starter circuits. When switching on the supply voltage, the large $68\,\mu\mathrm{F}$ capacitors slowly open the transistors on a time-scale $\tau = RC = 147\,\mathrm{ms}$ to minimize VCO noise from suddenly turning it on. A 3 dB attenuator was included to match the VCO output power to the reference power.

6.3.2 Output

Typical spectral traces of the box' output are shown in Fig. 6.6. These scans were taken while using the Cs-referenced DDS oscillator described in Sec. 6.4 at 50 MHz as a reference to produce a signal at 1 GHz (multiplication factor 20). Each scan uses a smaller scan to zoom in on the center frequency, until the minimal bandwidth of 100 Hz is reached in Fig. 6.6(c) which was taken with the max-hold setting over more than 60 s. Note that the spectrum analyzer was not calibrated, the signal is at 1 GHz with the

accuracy of the 10 MHz signal produced by the Cs standard. The broad underground especially apparent in Fig. 6.6(c) is due to using the relatively inexpensive Minicircuits VCO. For the current experiment, the quality of the output sufficed, but higher quality wide-band VCOs[6] will be used in the next version of the circuit, promising to improve the spectrum drastically.

6.3.3 Software

Programming the ADF4111 requires a communication protocol called SPI which is a four-wire serial protocol. The library implements this protocol on the I/O pins of the USB board. The protocol timing is shown in Fig. 6.7: A zero on the CE (chip enable) pin shuts down the chip's output and resets all registers. Then, the program produces a clocking signal on the SCLK (serial clock) pin, causing the ADF4111 chip to read a bit from DATA on each rising edge. Finally, the transfer is completed by strobing LE (latch enable) telling the receiver to latch the accumulated data from its input buffer into the core. A rising edge on CE enables the chip again and completes the SPI transfer.[7]

A program is provided that uses the above protocol to expose all ADF4111 registers to the script language Lua[8] to simplify modification of parameters. A script that completely configures the device is shown in Lst. 6.1 (everything after "`--`" up to the end of the line is considered a comment).

```
-- pll.lua

-- USB I2C I/O serial number and bitmasks for pins
serial = "05070303"
sclk   = 0x00000010
data   = 0x00000020
le     = 0x00000040
ce     = 0x00000008

-- Data to write
f_latch = {0x12,0x00,0x02}
r_latch = {0x00,0x00,0x00}
n_latch = {0x00,0x00,0x01}

-- Do something to the data
-- ...

-- Power down the device, write data, power up
lib = ADF4111.new(sclk,data,le,ce,serial)
lib:ce(0)
lib:write(f_latch)
lib:write(r_latch)
lib:write(n_latch)
lib:ce(1)
```

[6] E.g. the VCO-107TC available from `http://www.sirenza.com`

[7] This is not a standard SPI transfer: usually, the CE pin is replaced with a CS (chip select) pin using negative logic. The device will not be turned off by a falling edge on CS but will not accept data otherwise. This allows omitting multiple versions of the SCLK, DATA and LE wires.

[8] Lua is a fast embeddable script language with low memory footprint, see `http://www.lua.org`.

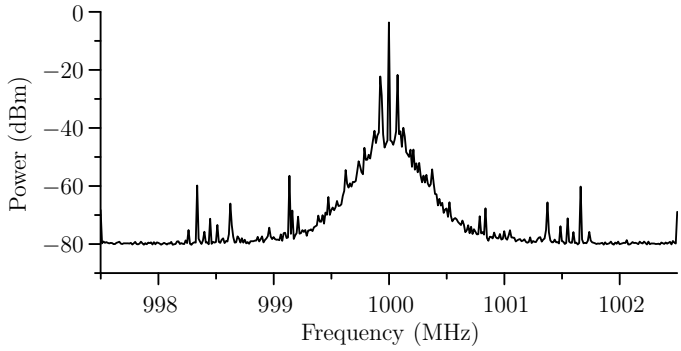

(a) bandwidth 1 kHz

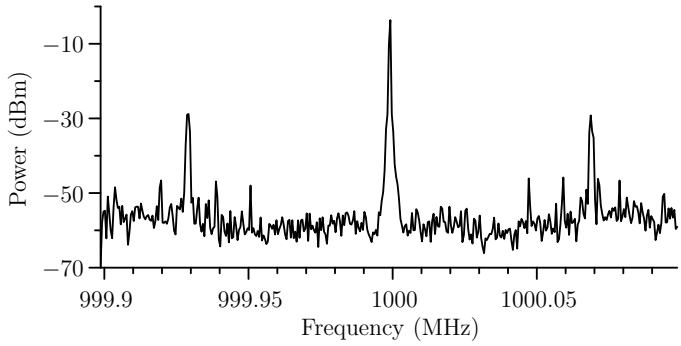

(b) bandwidth 100 Hz

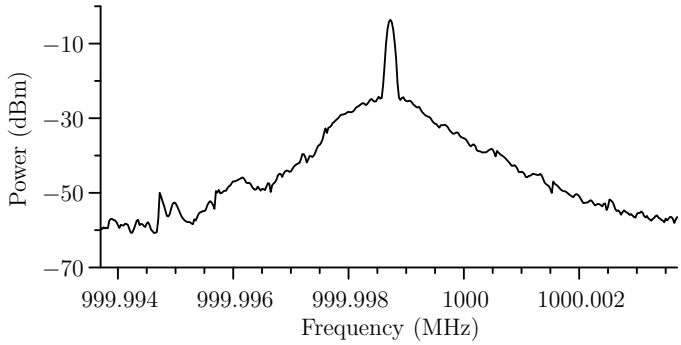

(c) max-hold >60 s, bandwidth 100 Hz

Figure 6.6: Spectral traces from the output of the frequency multiplier box producing a signal at 1 GHz. The traces zoom in on the peak; note that the spectrum analyzer was not calibrated and that the signal is at the specified 1 GHz with the accuracy of the reference used.

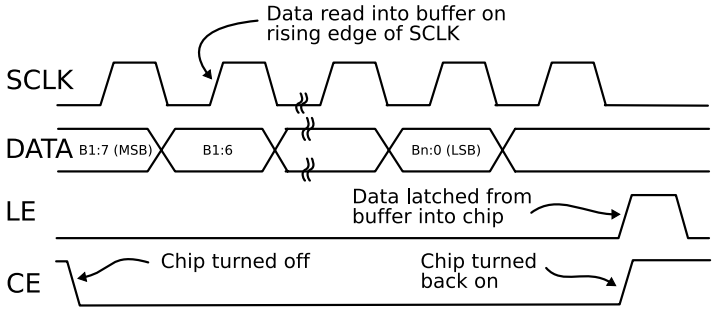

Figure 6.7: SPI data transfer protocol; used to transfer data from the controlling computer to the ADF4111 PLL chip

```
-- pll.lua ends here
```

Listing 6.1: Example Lua script for ADF4111.

A script like the above is executed by calling the embedded LUA interpreter with the script's path as argument: `interp.exe pll.lua`.

6.4 Direct Digital Synthesis

Direct digital synthesis (DDS) is a method to produce phase-continuous wave forms while tuning the synthesized frequency. In analog synthesizers, this is not possible as they use different phase-locked loops with specific frequency bands internally, causing the phase and even amplitude to jump when switching bands. When using the synthesized frequency as e.g. a moving reference for a phase-locked loop, this behavior will cause the lock to break. These analog devices are also very large and expensive. DDS offers a compelling alternative, as the synthesizers become much smaller, more effective and cheaper. They are also easier to program, since the whole board has to use CMOS logic anyway.

A DDS synthesizer has an internal array of memory that is filled with phase information. The chip then iterates over this array and produces a sine wave with corresponding phase at the output. Modifying the output frequency is as easy as modifying the iteration speed. The iteration speed is a fraction of the DDS chip's reference clock, making the synthesized frequency as accurate and stable as the reference clock is.

Commercial DDS systems that can be programmed via the GPIB bus are available from Agilent[9]. They are still quite expensive, and not very flexible in their programmability. We were looking for a DDS system able to fulfill the following list of requirements:

- Target frequency range: 50-100 MHz
- Must be referenced to 10 MHz Cs standard
- Able to produce linear frequency ramps with small slopes ($10\,^{\mathrm{Hz}}/_{\mathrm{s}}$) over long time scales (a whole day)

[9] E.g. the 80 MHz Agilent 33250A, see `http://www.home.agilent.com`

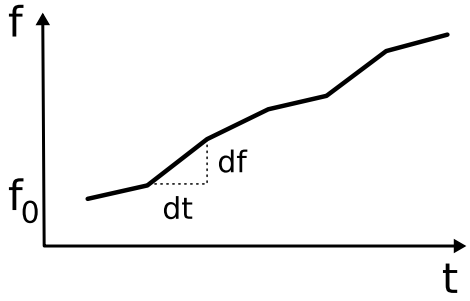

Figure 6.8: Piecewise linear frequency ramp

- Controllable with a Labview script to integrate well into the existing data acquisition system
- Support USB, since GPIB is too complicated and slow and RS232 or the parallel port are not flexible enough
- More than one DDS system can be connected to the same computer
- The whole system should cost much less than a commercial one, which retail for about USD 4500 at the moment

The most promising candidate was the Analog Devices AD9854 DDS chip[10], supporting reference frequencies up to 300 MHz. Evaluation boards with convenient SMC connectors are available for USD 300, so designing a high frequency printed circuit board was not necessary. The same USB digital I/O card (costs USD 80) as for the PLL frequency multiplier from Sec. 6.3 was used; the implementation of the chip's specific requirements was done by modifying the existing library. Labview bindings were written by wrapping calls to library functions in separate sub-VIs.

6.4.1 AD9854

The AD9854 has an on-chip phase-locked loop which can multiply the reference clock frequency by a programmable integer from 4 to 20. Using the 10 MHz Cs reference, this provides us with a virtual reference clock of 200 MHz. The DDS output frequency is limited by the Nyquist criterion, i.e. $f_{\text{out}} \leq f_{\text{ref}}/2$. We operate the DDS system at roughly 75 MHz, so this multiplication factor proved sufficient.

The DDS features different frequency modulation and ramping schemes; in our case we are using it in a piecewise linear fashion by setting the starting frequency once to 75 MHz and then updating the ramp slope, which is about $10\,{}^{\text{Hz}}/_{\text{s}}$ every 30 s.

This will produce a signal as in Fig. 6.8 where the frequency increment per f_{ref} cycle and the update interval in f_{ref} cycles are set in software.

Typical spectra of the output are presented in Fig. 6.9 for various output frequencies with and without on-chip reference clock multiplier. The output frequency was tuned to show why there is a huge sideband to the right of the intended output frequency (figures (a)) and to determine whether the background depends on the DDS board's settings

[10] See `http://www.analog.com`

(figures (b)). For all scans presented, the board was referenced to a 10 MHz Cs clock and the spectrum analyzer's bandwidth is noted in the figure caption. The (b) spectra were taken with the spectrum analyzer's max-hold setting turned on for more than a minute. Note that the (b) figures are still bandwidth limited, even at the lowest setting of 100 Hz and that the background only deteriorates a bit when turning on the reference clock multiplier.

In Fig. 6.9(a), the reference clock was multiplied up by a factor of 20 using the onchip PLL multiplier to produce a virtual reference of 200 MHz. In the subsequent (a) scans, this multiplier was turned off and the output frequency was tuned from 4 MHz to 1 MHz, covering a large range of the output between DC and the Nyquist frequency $f_{\mathrm{Ny}} = f_{\mathrm{ref}}/2 = 5\,\mathrm{MHz}$. The large sideband to the right of the main peak is the beat between the output frequency and the reference clock.

6.4.2 Caveats

There are several caveats that should be mentioned. Improvements and possible solutions are presented, but most have not been implemented as the system works sufficiently well.

The chip produces sidebands on the output signal as a beat between the various system frequencies: 10 MHz reference, 200 MHz virtual reference and 75 MHz output (see Figs. 6.9(a), 6.9(c), 6.9(e) and 6.9(g)). These sidebands have to be filtered out so the output signal is amplified and band-pass filtered before being used in the experiment.

The driver for the USB board is supplied by the manufacturer[11] and writes a single bit mask to the digital I/O pins per command. Since the DDS board uses a serial SPI protocol as well, transferring one bit takes 2 USB commands plus 4 control commands per write. To configure the device completely from scratch, at least 20 bytes have to be transferred. The time it takes to perform one write operation is limited by the operating system's time resolution: ∼4 ms for a typical 32 bit Windows system. That means that writing to the DDS system is very costly and several optimizations were included to limit the number of bytes written on each update to the bare minimum. Still, it takes almost a second to update the slope data. During this time the DDS continues ramping using its old settings as the data is buffered and then latched into the chip. The problem is that updating more often than every few seconds will not work with the current setup. In our experiment this does not matter currently, since the update cycle is limited by how much data can be obtained during one cycle. At the moment, a 30 s update cycle is used.

This problem could be eliminated by writing a custom USB driver for the chip used on the USB I/O board — a Cypress EZUSB microcontroller[12]. Another more powerful solution would be to include some logic chips in the DDS system, like a sufficiently advanced microprocessor running a real-time operating system. This would allow arbitrary programs to be written which could be executed with a much faster update rate.

[11] Driver available for download at `http://www.devasys.com`.
[12] See `http://www.cypress.com`

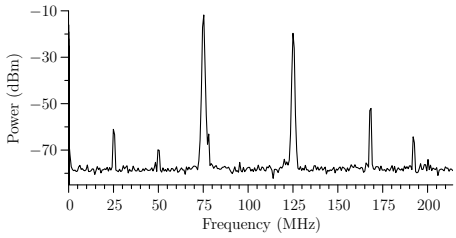

(a) 75 MHz, multiplier ×20, bandwidth 10 kHz

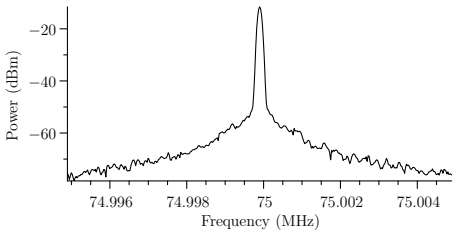

(b) 75 MHz, multiplier ×20, max-hold >60 s, bandwidth 100 Hz

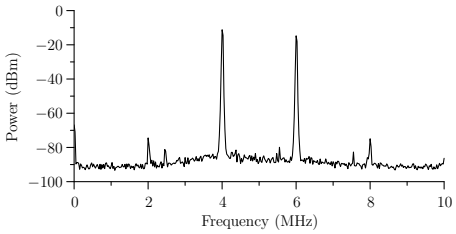

(c) 4 MHz, multiplier off, bandwidth 10 kHz

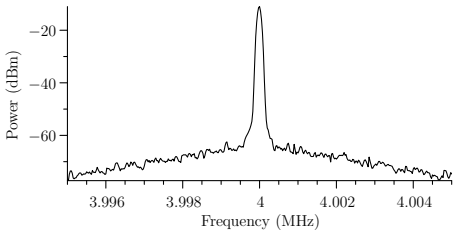

(d) 4 MHz, multiplier off, max-hold >60 s, bandwidth 100 Hz

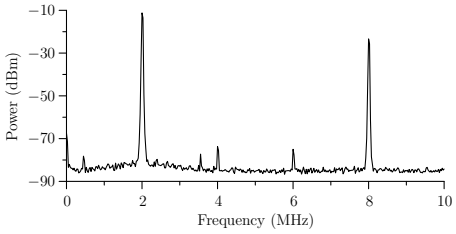

(e) 2 MHz, multiplier off, bandwidth 10 kHz

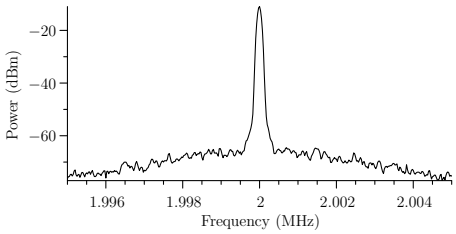

(f) 2 MHz, multiplier off, max-hold >60 s, bandwidth 100 Hz

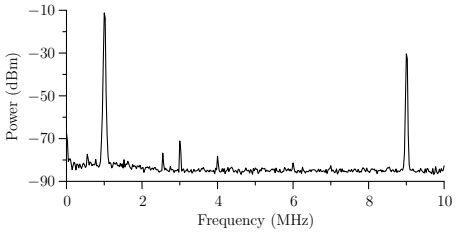

(g) 1 MHz, multiplier off, bandwidth 10 kHz

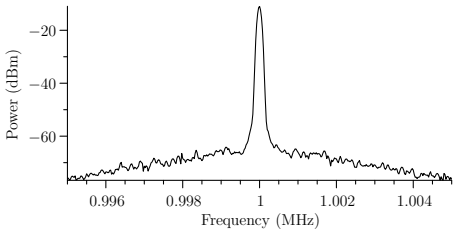

(h) 1 MHz, multiplier off, max-hold >60 s, bandwidth 100 Hz

Figure 6.9: AD9854 DDS spectral traces for different output frequencies

An interesting candidate would be an ARM microprocessor[13] running µClinux[14]. This would also require that relevant data could be read directly by the microprocessor; thus adding some analog or digital inputs to the DDS system would be necessary.

Another bonus of this more advanced and work-intensive approach would be that the system is fast and stable enough so that arbitrary non-linear frequency ramps and pulse sequences could be synthesized — with a precision limited only by the reference clock.

6.4.3 Software: Drift Compensation

To compensate the residual mechanical drift rate, the DDS system has to be programmed to emit a frequency ramp. The system is based on Labview and uses a HP53132a counter to count the beat between NIST's hydrogen maser and the femtosecond comb which is locked to the spectroscopy laser. By measuring this beat frequency over a time interval τ, the program obtains an array of frequency data, to which a linear function is fitted. The slope in Hz/s corresponds directly to the mechanical drift rate of the cavity. The box is then programmed to emit a frequency slope to compensate for the drift. The program retains knowledge of all prior slope settings and can use them along with the newest fitted slope to form a new slope value. By calculating a weighted mean of the latest n slopes, the loop filter simulates the memory time of an analog circuit. Safeguards are included to protect against outliers and sudden jumps in laser frequency due to breaking locks. Screenshots of the controls are shown in Fig. 6.10: All parameters determining the behavior of the digital loop filter can be adjusted with the first panel (Fig. 6.10(b)), real-time display and analysis is shown below (Fig. **??**).

One of the first drift compensation measurements is depicted in Fig. 6.11(a). Initially, the optical frequency is drifting at a large rate; after 2 min, the device manages to keep the optical frequency within several hundred Hz for half an hour. The Allan deviation of this frequency measurement is plotted below, averaging down to a relative instability of 10^{-13} at 20 s.

The maximum time of a continuous drift compensation run is limited by the laser systems becoming unlocked. The Allan deviation is mostly determined by the instability of the hydrogen maser. The digital loop filter was improved by adding an integration step in analogy to the memory time of an analog filter. This allowed averaging down the instability faster as can be seen in the considerably longer compensation run in Fig. 6.11(b), reaching 7×10^{-14} at 70 s.

A typical spectrum of the ${}^1S_0 - {}^3P_0$ transition takes about 100 s, so the optical frequency maximally drifts by ~ 30 Hz, which proved to be sufficient for the current experiment. The sign of the cavity's drift stayed the same for several months and the average rate was always between 4 and 9 Hz. The spectral scans were taken alternating the direction of the scan each time; viz. alternatively with increasing and decreasing frequency. Since the linewidth did not show any dependency on the direction of the

[13] E.g. Atmel AT91 ARM series, see `http://www.atmel.com`

[14] A real-time Linux operating system with ports for a variety of microprocessors and -controllers. See `http://www.uclinux.org`

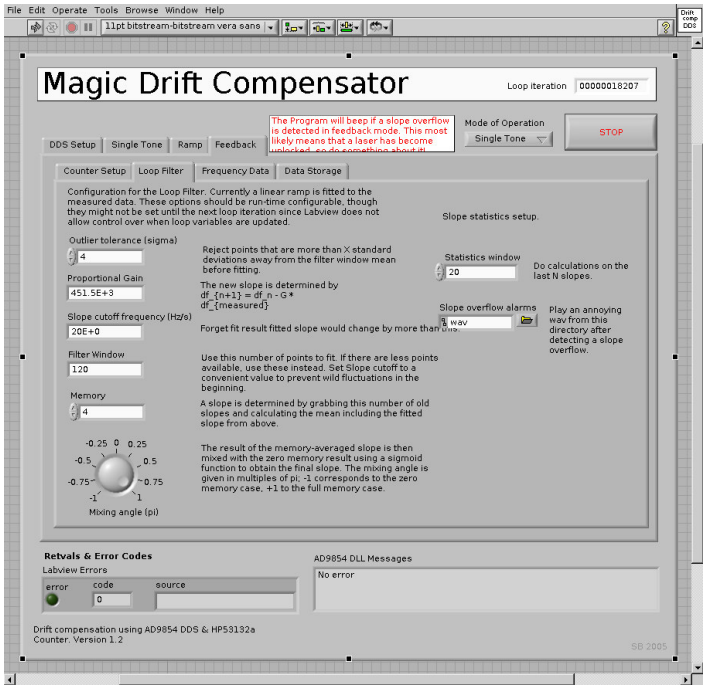

(a) Digital loop filter setup

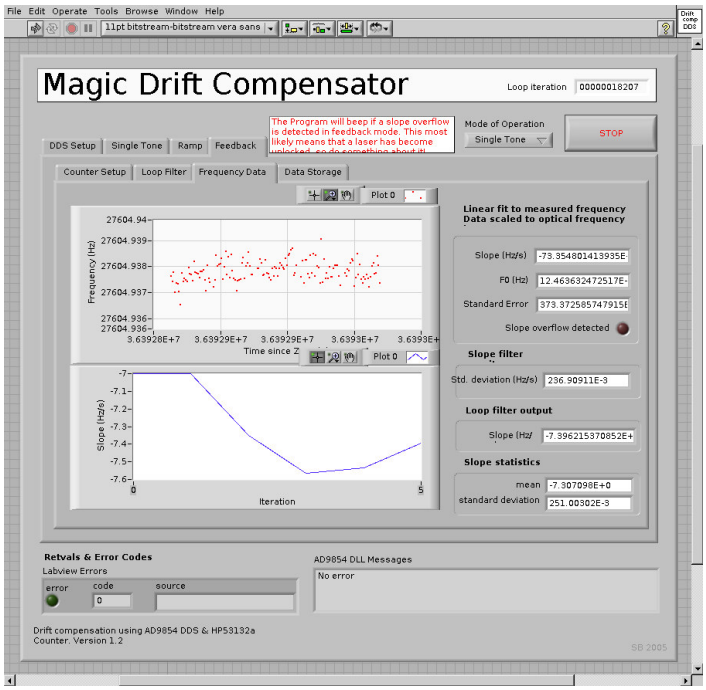

(b) Compensation run

Figure 6.10: Drift compensation screenshots

scan, we are confident that the drift compensation does not have any effect on our data at the current resolution.

In future work, the drift compensation will work as an aside to help maintain the correct frequency, but the spectra will be referenced to the atomic transition itself.

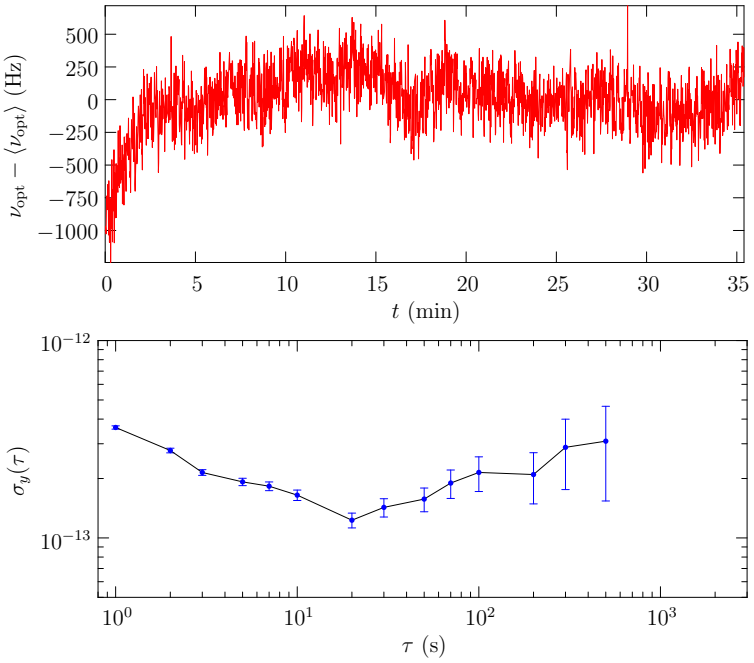

(a) Early drift compensation run

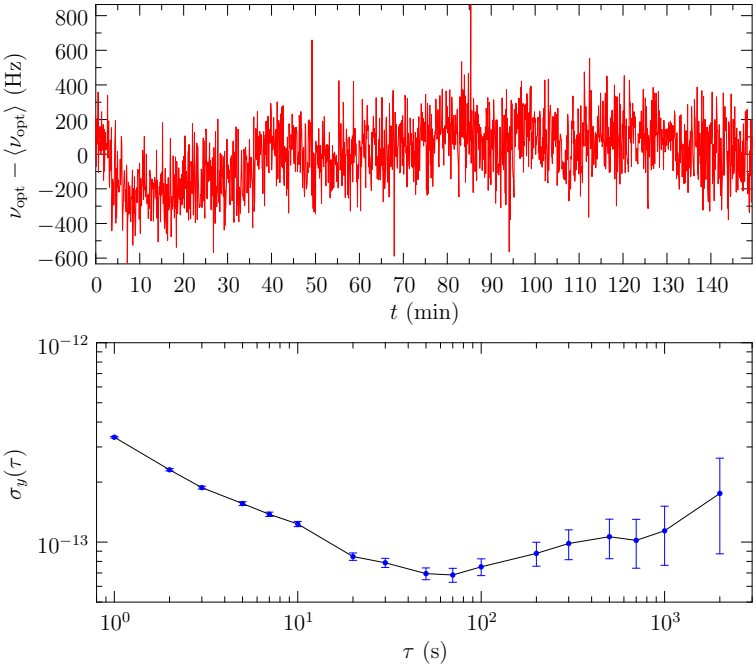

(b) Improved digital loop filter

Figure 6.11: Drift compensation data and Allan deviation

Chapter 7

Results and Outlook

The first spectroscopic measurement of the $^1S_0 - {}^3P_0$ clock transition in ^{87}Sr was reported by the Tokyo group (Takamoto *et al.*, 2005). We presented an second independent measurement, experimentally determining important systematics (instead of giving theoretical estimates) and achieving a better statistical accuracy. We report a $^1S_0 - {}^3P_0$ transition frequency of $(429\,228\,004\,229\,867 \pm 20\ \mathrm{sys} \pm 2.8\ \mathrm{stat})$ Hz, disagreeing with the Tokyo group's result by 85 Hz. The results of the Tokyo group and our measurement are compared in Fig. 7.1, where the blue (red) bars indicate systematic (statistical) errors. Their GPS-referenced measurement (instability $\sim 10^{-10}$ @ 1 s) would have required averaging times of more than 10^6 s to achieve the reported instability of 3×10^{-14} (this was not done). In contrast, we used a hydrogen-maser referenced itself to NIST's F1 Cs-fountain clock: A reference that has an instability of 2×10^{-13} @ 1 s and typically shows instabilities of 7×10^{-14} at our scan time of 100 s (see Fig. 6.11(b)). A budget of the error sources discussed in sections 4.6 and 5.3 is summarized in Tbl. 7.1.

The drift compensation scheme presented in this work allowed compensating for an unstable reference cavity while maintaining various laser locks. This made it possible to consistently measure spectra below the 200 Hz level, almost achieving the quantum

Contributor	Correction (Hz)	Uncertainty (Hz)	Section in this work
AC Stark shift (lattice)	-17	8.3	5.3 on page 45
AC Stark shift (probe)	7.0	0.9	4.6.2 on page 34
AC Stark shift (blackbody)	2.4	0.02	4.6.3 on page 36
Zeeman shift	0	12	5.3 on page 45
Recoil / Doppler shift	0	1.9	5.2 on page 43
Density shift	-2.0	13	5.3 on page 45
Gravitational shift	-0.64	0.13	4.6.5 on page 39
Cs-maser calibration	46.8	0.5	(Data from NIST)
Systematic total	36	20	

Table 7.1: Error budget for $^1S_0 - {}^3P_0$ spectroscopy, modified from Ludlow *et al.* (2005)

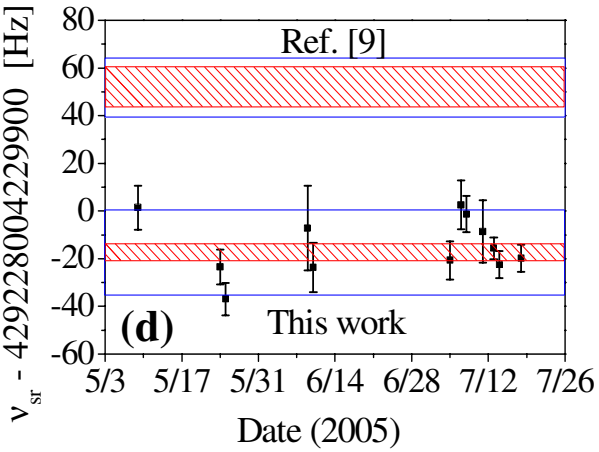

Figure 7.1: Comparison of results from Takamoto *et al.* (2005) (upper part) and Ludlow *et al.* (2005) (lower part), figure from the latter paper

mechanical uncertainty limit of 50 Hz for the current 1D optical lattice setup. We also demonstrated an unprecedented level of control on large timescales of an all optical trap for neutral atoms, allowing measurements previously only doable for ions such as vibrational spectroscopy. In contrast to the ion trap experiments, the anharmonicity of the optical potential and its matched shape for both spectroscopic levels allow state-resolved studies of vibrational dissipation. A semi-classical model describing the effect of external noise sources has been given in this work.

In future experiments, the spectroscopic scans will be referenced directly to the $^1S_0 - {}^3P_0$ transition. The 1D lattice will be replaced by a three-dimensional version, promising to eliminate several systematics such as the aforementioned uncertainty limit as well as the tensorial polarizability of the electronic states.

A scheme to use ^{88}Sr for an optical lattice clock by simulating the ultranarrow $^1S_0 - {}^3P_0$ transition in an *Electromagnetically-Induced Transparency* (EIT) scheme has been proposed by Santra *et al.* (2005). Using the bosonic ^{88}Sr would remove all the hyperfine structure effects and the EIT scheme would provide a controllable transition width. Alternatively, measuring the ^{87}Sr hyperfine constants with the current precision could improve the understanding of hyperfine mixing by providing the theory with more parameters.

The current setup also allows *photo-associative spectroscopy* (PAS) experiments which will lead to better understanding of the ^{87}Sr two-body interactions, such as getting a measure of the scattering length. PAS has never been done on such a narrow line as the ^{87}Sr $^1S_0 - {}^3P_0$ transition, although several groups have demonstrated PAS on the singlet transition $^1S_0 - {}^1P_1$ in ^{88}Sr (Nagel *et al.*, 2005, Yasuda *et al.*, 2005). Work on this narrow-line PAS is in progress.

All these experiments and improvements will help further understanding atomic strontium and alkaline earths in general. The all optical atomic clock with an instability of 10^{-18} is an important application, but by far not the only one. The ultrahigh precision

and low instability required for these experiments also opens up completely new fields, such as the possibility to test the evolution of fundamental constants such as the fine structure constant α.

Bibliography

Abramowitz, Milton and Irene A. Stegun, eds.
Handbook of Mathematical Functions (Dover, 1972)

Adams, C.S. and E. Riis.
Laser cooling and trapping of neutral atoms.
Prog. Quant. Electr. **21**, p. 1 (1997)

Allan, David W., Neil Ashby and Clifford C. Hodge.
Application note 1289: The science of timekeeping.
Hewlett Packard Application Notes (1997)

Bransden, B. H. and C. J. Joachain.
Physics of Atoms and Molecules.
2nd edn. (Prentice Hall, 2003)

Breit, G. and Lawrence A. Wills.
Hyperfine structure in intermediate coupling.
Phys. Rev. **44**(6), pp. 470–490 (1933)

Brink, D. M. and G. R. Satchler.
Angular Momentum.
2nd edn. (Clarendon Press, Oxford, 1968)

Dicke, R. H.
The effect of collisions upon the Doppler width of spectral lines.
Phys. Rev. **89**(2), pp. 472–473 (1953)

Fortier, T. M., David J. Jones and S. T. Cundiff.
Phase stabilization of an octave-spanning Ti:sapphire laser.
Opt. Lett. **28**(22), pp. 2198–2200 (2003)

Franklin, Gene F., J. David Powell and Abbas Emami-Naeni.
Feedback Control of Dynamic Systems.
3rd edn. (Addison-Wesley, 1994)

Gardiner, C. W., J. Ye, H. C. Nägerl and H. J. Kimble.
Evaluation of heating effects on atoms trapped in an optical trap.
Phys. Rev. A **61**, pp. 045801–1 (2000)

Gardiner, Crispin W.
Handbook of Stochastic Methods.
3rd edn. (Springer, 2004)

Gibble, Kurt and Steven Chu.
Laser-cooled Cs frequency standard and a measurement of the frequency shift due to ultracold collisions.
Phys. Rev. Lett. **70**(12), pp. 1771–1774 (1993)

Hall, John L., Matthew S. Taubman and Jun Ye.
Fiber Optics & Nonlinear Optics, vol. IV of *Handbook of Optics*, chap. 27, pp. 27.1–27.23.
2nd edn. (McGraw-Hill, 2001)

Heider, Stephan M. and Gilbert O. Brink.
Hyperfine structure of ^{87}Sr in the $^3P_2$ metastable state.
Phys. Rev. A **16**(4), pp. 1371–1374 (1977)

Heuser, Harro.
Gewöhnliche Differentialgleichungen. Einführung in Lehre und Gebrauch (Teubner, 1995)

Ido, Tetsuya, Thomas H. Loftus, Martin M. Boyd, Andrew D. Ludlow, Kevin W. Holman and Jun Ye.
Precision spectroscopy and density-dependent frequency shifts in ultracold Sr.
Phys. Rev. Lett. **94**, p. 153001 (2005)

Itano, W. M., J. C. Bergquist, J. J. Bollinger, J. M. Gilligan, D. J. Heinzen, F. L. Moore, M. G. Raizen and D. J. Wineland.
Quantum projection noise: Population fluctuations in two-level systems.
Phys. Rev. A **47**(5), pp. 3554–3570 (1993)

Jáuregui, R.
Nonperturbative and perturbative treatments of parametric heating in atom traps.
Phys. Rev. A **64**, p. 053408 (2001)

Jáuregui, R., N. Poli, G. Roati and G. Modugno.
Anharmonic parametric excitation in optical lattices.
Phys. Rev. A **64**, p. 033403 (2001)

Katori, H.
In *Proceedings of the 6th Symposium on Frequency Standards and Metrology*, edited by P. Gill, pp. 323–330 (World Scientific, 2002)

Kimble, H. J., C. J. Hood, T. W. Lynn, H. Mabuchi, D. W. Vernooy and J. Ye.
The quantum internet.
In *Proceedings of the Fourteenth International Conference on Laser Spectroscopy (ICOLS99), Innsbruck*, edited by R. Blatt, J. Eschner, D. Leibfried and F. Schmidt-Kaler, pp. 80–89 (World Scientific, 1999)

Legere, Ronald and Kurt Gibble.
Quantum scattering in a juggling atomic fountain.
Phys. Rev. Lett. **81**(26), pp. 5780–5783 (1998)

Lesage, P. and F. Audoin.
Characterization of frequency stability: uncertainty due to the finite number of measurements.
IEEE Trans. Instr. Meas. **IM-22**, p. 103 (1973)

Loftus, T. H., T. Ido, A. Ludlow, M. M. Boyd and J. Ye.
Narrow line cooling and momentum-space crystals.
Phys. Rev. A **70**(6), pp. 063413/1–14 (2004a)

—.
Narrow line cooling: finite photon recoil dynamics.
Phys. Rev. Lett. **93**(7), pp. 073003/1–4 (2004b)

Loudon, Rodney.
The quantum theory of light.
2nd edn. (Oxford University Press, 1983)

Ludlow, Andrew D., Martin M. Boyd, T. Zelevinsky, Seth M. Foreman, Sebastian Blatt, Mark Notcutt, Tetsuya Ido and Jun Ye.
Systematic study of the ^{87}Sr clock transition in an optical lattice.
Phys. Rev. Lett. **(submitted)** (2005)

Lurio, A., M. Mandel and R. Novick.
Second-order hyperfine and Zeeman corrections for an (sl) configuration.
Phys. Rev. **126**(5), pp. 1758–1767 (1962)

Merzbacher, Eugen.
Quantum Mechanics.
3rd edn. (Wiley, 1998)

Metcalf, Harold J. and Peter van der Straten.
Laser Cooling and Trapping (Springer, 1999)

Moore, C. E.
Atomic Energy Levels, vol. I-III (NSRDS, 1971)

Mukaiyama, Takashi, Hidetoshi Katori, Tetsuya Ido, Ying Li and Makoto Kuwata-Gonokami.
Recoil-limited laser cooling of ^{87}Sr atoms near the Fermi temperature.
Phys. Rev. Lett. **90**(11), p. 113002 (2003)

Nagel, S. B., P. G. Mickelson, A. D. Saenz, Y. N. Martinez, Y. C. Chen, T. C. Killian, P. Pellegrini and R. Côté.
Photoassociative spectroscopy at long range in ultracold strontium.
Phys. Rev. Lett. **94**(8), p. 083004 (2005)

Nash, Garth.
AN535: Phase-locked loop design fundamentals.
Motorola Semiconductor Application Notes (1994)

Notcutt, Mark, Long-Sheng Ma, Jun Ye and John L. Hall.
Simple and compact 1-Hz laser system via an improved mounting configuration of a reference cavity.
Opt. Lett. **30**(14), pp. 1815–1817 (2005)

Paredes, Belén, Artur Widera, Valentin Murg, Olaf Mandel, Simon Fölling, Ignacio Cirac, Gora V. Shlyapnikov, Theodor W. Hänsch and Immanuel Bloch.
Tonks-Girardeau gas of ultracold atoms in an optical lattice.
Nature **429**, pp. 277–281 (2004)

Peik, E., G. Hollemann and H. Walther.
Laser cooling and quantum jumps of a single indium ion.
Phys. Rev. A **49**, pp. 402–408 (1994)

Poli, N., R. J. Brecha, G. Roati and G. Modugno.
Cooling atoms in an optical trap by selective parametric excitation.
Phys. Rev. A **65**, p. 021401(R) (2002)

Porsev, Sergey G. and Andrei Derevianko.
Hyperfine quenching of the metastable $^3P_{0,2}$ *states in divalent atoms.*
Phys. Rev. A **69**, p. 042506 (2004)

Risken, Hannes.
The Fokker-Planck Equation: Methods of Solutions and Applications.
2nd edn. (Springer, 1996)

Rotenberg, Manuel, R. Bivins, N. Metropolis and John K. Wooten, Jr.
The 3-j and 6-j symbols (The Technology Press, Massachusetts Institute of Technology, 1959)

Sakurai, J. J.
Modern Quantum Mechanics.
Revised edn. (Addison-Wesley, 1994)

Santarelli, G., Ph. Laurent, P. Lemonde, A. Clairon, A. G. Mann, S. Chang, A. N. Luiten and C. Salomon.
Quantum projection noise in an atomic fountain: A high stability cesium frequency standard.
Phys. Rev. Lett. **82**(23), pp. 4619–4622 (1999)

Santra, Robin, Ennio Arimondo, Tetsuya Ido, Chris H. Greene and Jun Ye.
High-accuracy optical clock via three-level coherence in neutral bosonic ^{88}Sr.
Phys. Rev. Lett. **94**(17), p. 173002 (2005)

Savard, T. A., K. M. O'Hara and J. E. Thomas.
Laser-noise-induced heating in far-off resonance optical traps.
Phys. Rev. A **56**, p. R1095 (1997)

Stenholm, Stig.
The semiclassical theory of laser cooling.
Rev. Mod. Phys. **58**, p. 699 (1986)

Sullivan, D. B., D. W. Allan, D. A. Howe and F. L. Walls, eds.
Characterization of Clocks and Oscillators.
No. 1337 in NIST Technical Notes (NIST, 1990)

Takamoto, Masao, Feng-Lei Hong, Ryoichi Higashi and Hidetoshi Katori.
An optical lattice clock.
Nature **435**, pp. 321–324 (2005)

Werij, H. G. C., Chris H. Greene, C. E. Theodosiou and Alan Gallagher.
Oscillator strengths and radiative branching ratios in atomic Sr.
Phys. Rev. A **46**(3), pp. 1248–1260 (1992)

Wineland, D. J. and Wayne M. Itano.
Laser cooling of atoms.
Phys. Rev. A **20**, p. 1521 (1979)

Xu, Xinye, Thomas H. Loftus, Josh W. Dunn, Chris H. Greene, John L. Hall, Alan Gallagher and Jun Ye.
Single-stage sub-Doppler cooling of alkaline earth atoms.
Phys. Rev. Lett. **90**(19), pp. 193002/1–4 (2003a)

Xu, Xinye, Thomas H. Loftus, John L. Hall, Alan Gallagher and Jun Ye.
Cooling and trapping of atomic strontium.
J. Opt. Soc. Am. B **20**(5), pp. 968–976 (2003b)

Xu, Xinye, Thomas H. Loftus, Matthew J. Smith, John L. Hall, Alan Gallagher and Jun Ye.
Dynamics in a two-level atom magneto-optical trap.
Phys. Rev. A **66**, p. 011401(R) (2002)

Yasuda, Masami, Tetsuo Kishimoto, Masao Takamoto and Hidetoshi Katori.
Wave-function reconstruction for the determination of the scattering length of Sr.
arxiv:physics/0501053 (2005)

Ye, Jun and Steven T. Cundiff, eds.
Femtosecond Optical Frequency Comb: Principle, Operation and Applications (Springer, 2004)

Ye, Jun, Jin-Long Peng, R. Jason Jones, Kevin W. Holman, John L. Hall, David J. Jones, Scott A. Diddams, John Kitching, Sebastien Bize, James C. Bergquist, Leo W. Hollberg, Lennart Robertsson and Long-Sheng Ma.
Delivery of high-stability optical and microwave frequency standards over an optical fiber network.
J. Opt. Soc. Am. B **20**(7), pp. 1459–1467 (2003)

Index

6j-symbol, 22

AC-Stark shift, 15
Acousto-Optical Modulators, 41
Allan deviation, viii, 3
Allan variance, 1, 3
AOMs, *see* Acousto-Optical Modulators

blackbody shift, 36
Bode plot, 10
Bohr magneton, 37
Bohr radius, 36

characteristic exponent, 26
Clebsch-Gordan coefficients, 37
convolution, 9

DDS, *see* Direct digital synthesis
dead time, 2
detuning, 16
Direct digital synthesis, 63
DMOT, *see* Dynamic MOT
Doppler effect, 16
    second order, 34
Doppler temperature, 17
Dynamic MOT, 19

ECDLs, *see* External Cavity stabilized Diode Lasers
effective magnetic moment, 18
Einstein A coefficient, 16
EIT, *see* Electromagnetically-Induced Transparency
Electromagnetically-Induced Transparency, 72
External Cavity stabilized Diode Lasers, 43

feedback loop, 5
    forward gain, 6
    loop gain, 6
Floquet solutions, 26
Fokker-Planck equation, 15

gate time, 2
global positioning system, vii
GPS, *see* global positioning system
Green's function, 6

Hartree energy, 36

Lamb-Dicke parameter, 28
Lamb-Dicke regime, 28
LO, *see* local oscillator
local oscillator, 5

magic wavelength, 24
Magneto-Optical Trap, 17
Mandel Q-parameter, 17
Maxwell-Boltzmann, 33
    probability density function, 33
MOT, *see* Magneto-Optical Trap

nominal frequency, 1

one-sided Laplace transform, 6
optical atomic clock, viii
optical lattice, 21

PAS, *see* photo-associative spectroscopy
PD, *see* phase detector
PFD, *see* phase-frequency detector
phase detector, 9
phase-frequency detector, 10
phase-locked loop, 4
    analog mixer, 7
    bandwidth, 10
    capture range, 10
    loop filter, 7
photo-associative spectroscopy, 72
photo-multiplier tube, 41
PLL, *see* phase-locked loop
PMT, *see* photo-multiplier tube

reduced matrix elements, 22

saturation intensity, 16
saturation parameter, 16
SI, *see* système international
système international, vii

time deviation, 2
Tonks-Girardeau gas, 50
transfer function, 5

VCO, *see* voltage-controlled oscillator
voltage-controlled oscillator, 4

Wannier basis, 26
Wigner-Eckart theorem, 22

Zeeman effect
    diamagnetic term, 37
    second order, 37
Zeeman splitting, 17

Acknowledgements

Many people have directly and indirectly contributed to this text: I thank Rudi Grimm for accepting me as a diploma student and Jun Ye for making my work at JILA possible, as well as supporting and encouraging me along the way. I learned a great deal about what can be achieved with the right idea.

My special thanks go to all the members of the Sr Gang (in alphabetical order: Marty Boyd, Seth Foreman, Tetsuya Ido, Andrew Ludlow and Tanya Zelevinsky) for letting me play with the most sensitive parts of their increasingly complex setup. You provided a great work atmosphere and were always ready to help.

I also want to mention the amazing members of the JILA electronics shop, especially Terry Brown and James Fung-a-Fat who gave great advice and laid out all the printed circuit boards I used.

Without my parents' help and constant support all of this would never have been possible.